

# Retinomorphic Feature Detection and Machine Vision in a Network Laser

Wai Kit Ng<sup>1,†</sup>, Jakub Dranczewski<sup>1,2,†</sup>, Anna Fischer<sup>1,2,†</sup>, T. V. Raziman<sup>1,3</sup>, Dhruv Saxena<sup>1</sup>, Tobias Farchy<sup>1</sup>, Kilian Stenning<sup>1,4</sup>, Jonathan Peters<sup>1,5</sup>, Heinz Schmid<sup>2</sup>, Will R. Branford<sup>1,4</sup>, Mauricio Barahona<sup>3</sup>, Kirsten Moselund<sup>6,7</sup>, Riccardo Sapienza<sup>1,\*</sup>, and Jack C. Gartside<sup>1,5,\*</sup>

<sup>1</sup>Blackett Laboratory, Department of Physics, Imperial College London, London, United Kingdom

<sup>2</sup>IBM Research Europe – Zürich, Säumerstrasse 4, Rüschlikon, 8803, Switzerland

<sup>3</sup>Department of Mathematics, Imperial College London, London, United Kingdom

<sup>4</sup>London Centre for Nanotechnology, Imperial College London, London, United Kingdom

<sup>5</sup>Univ. Grenoble Alpes, CEA, CNRS, Grenoble INP, SPINTEC, France

<sup>6</sup>Laboratory of Nano and Quantum Technologies, Paul Scherrer Institut, Switzerland

<sup>7</sup>INPhO, Faculty of Engineering, Ecole Polytechnique Fédérale de Lausanne, Switzerland

\*Corresponding author e-mails: j.carter-gartside13@imperial.ac.uk, r.sapienza@imperial.ac.uk

## ABSTRACT

Biological vision systems seamlessly integrate feature-sensitive spatial processing and strong nonlinearity. The retina performs feature detection via ganglion cells, which nonlinearly enhance image features such as edges through lateral inhibition processes between neighbouring cells. As demand for specialised machine learning hardware increases, physical systems are sought which combine feature detection with the nonlinear processing required for tasks such as image classification. Currently, physical machine vision schemes detect features linearly, then employ separate digital systems for subsequent nonlinear activation.

Here, we introduce a bio-inspired ‘retinomorphic’ machine vision platform using a semiconductor network laser. The system hosts many spatially-overlapping lasing modes which detect multiple image features in parallel via their lasing amplitude. Integrated nonlinearity is provided by antagonistic competition for gain between modes - a photonic analogue of the lateral inhibition in retinal cells. Detected feature maps are fed back through the system, providing multi-layer image classification with intrinsic nonlinear processing. Accuracies of 98.05% and 87.85% are achieved for MNIST digits and Fashion-MNIST tasks respectively.

## Introduction

Machine learning and its benefits are increasingly ubiquitous across industry and society. However, they are accompanied by exponentially increasing energy and carbon costs. As conventional CMOS processors struggle to keep pace with the rising demands of machine learning, the need increases for dedicated hardware solutions that implement machine learning architectures.

An architecture with pressing need for such solutions is the convolutional neural network (CNN), widely used in machine vision<sup>1,2</sup>. Machine vision, where tasks such as feature detection, classification and segmentation are performed on image data, represents a significant portion of modern machine learning demand<sup>3,4</sup>. CNNs begin with a feature detection layer where convolutional kernel filters are raster-scanned across an image to build ‘feature maps’ of image features such as edges, corners and curves. Each kernel detects a single separate feature, with multiple kernels scanned sequentially to produce a set of feature maps. These feature maps are then processed via nonlinear activation and passed to a subsequent classification layer, typically fully-connected hidden layers including additional nonlinear activations. The initial convolutional feature detection greatly enhances machine vision performance relative to neural networks containing only multi-layer perceptron style hidden layers<sup>1-4</sup>.

While powerful, convolutional feature detection is computationally expensive<sup>5,6</sup>. As such, developing dedicated physical hardware which implements CNN functionality is an active research effort. Recent breakthroughs have seen impressive implementations of convolutional feature detection in physical systems including memristor arrays<sup>7</sup>, photonic integrated circuits<sup>8,9</sup> and meta-surfaces<sup>10</sup>, demonstrating the benefits of physical convolutional processing. These existing schemes adopt the structure of software CNNs - performing feature detection in a linear regime by implementing physical equivalents of the linear matrix multiplications used in software.

The drawback of such linear physical approaches is that they are unable to provide the crucial nonlinearity required for more complex machine vision tasks beyond feature detection, such as image classification. This is typically navigated by passing the detected feature maps to a digital CMOS computer which implements nonlinear activation in software<sup>11–13</sup>. Often, the software also performs the full classification process via a conventional deep neural network with additional nonlinear activations<sup>8,10</sup>. This is nonetheless excellent progress - convolutional feature detection is computationally expensive in software, hence appealing to offload to specialised physical systems.

Biological vision systems function quite differently to software CNNs. Biological feature detection directly integrates nonlinear processing rather than implementing it as a separate subsequent step, and multiple features are detected in parallel with nonlinear coupling between the detection processes<sup>14,15</sup> as opposed to the discrete kernel filters used in software CNNs. In the retina, feature detection is performed by retinal ganglion cells, the final output neurons in the retinal circuitry<sup>14</sup>. These cells utilise a process termed ‘lateral inhibition’ to nonlinearly enhance image features such as edges<sup>16–18</sup>. When a ganglion cell is activated, it sends excitatory signals to the brain while simultaneously sending inhibitory neurotransmitter signals to adjacent ganglion cells, decreasing the firing activity of neighbouring cells. This dynamic interplay between adjacent cells provides nonlinear enhancement of image edges, as the inhibition disproportionately affects cells receiving weaker stimuli (e.g., darker image regions). At the boundary between adjacent light and dark regions (e.g., an image edge), brightly illuminated ganglion cells strongly inhibit their weakly illuminated neighbours while receiving less inhibition themselves, thereby nonlinearly amplifying neuronal activity at image edges. Additionally, different subsets of ganglion cells respond preferentially to different angles and orientations of edges, allowing the retina to process complex images with multiple features in parallel<sup>14,15</sup>.

It is appealing to draw inspiration from biological architectures, and engineer physical platforms capable of detecting multiple features in parallel with integrated nonlinearity. Neuromorphic computing is an approach which takes this bio-inspired angle and aims to implement machine learning by leveraging the complex nonlinear dynamics of physical systems<sup>11,13,19</sup>. However, gaining fine control over the nonlinear physical dynamics powering neuromorphic computing is a subtle and challenging task, particularly for more sophisticated multi-layer learning architectures such as CNNs where each layer of the neuromorphic system must perform very different processing<sup>12,13</sup>. To date, a physical system integrating feature detection and physical nonlinearity remains unrealised to the best of our knowledge. Gaining enhanced control over nonlinear physical dynamics to realise such functional integration has been identified as a key goal for the field<sup>11–13</sup>.

In photonic systems, complex lasers which host many competing lasing modes<sup>20–22</sup> offer an inviting candidate system for implementing bio-mimetic machine vision. They provide nonlinear processing via lasing threshold dynamics and mode competition<sup>23–26</sup>, and provide spatial sensitivity through their responsive reaction to structured light<sup>23,24,26,27</sup>. Crucially, nonlinear mode competition for gain between overlapping modes provides an attractive photonic analogue of retinal lateral inhibition processes - offering routes to feature detection. These promising systems have not yet been explored for computation.

Here, we demonstrate a neuromorphic machine vision platform using a lithographically-patterned InP network laser<sup>28</sup>, fabricated through the mature process of wafer-bonding InP on oxide-coated Si<sup>29</sup>. InP is a well-established photonic platform suitable for active devices in the telecoms range and robust to degradation. By harnessing nonlinear mode competition, we engineer a bio-inspired ‘retinomorphic’ design where spatially-distributed lasing modes overlap throughout the network, competing for gain and suppressing neighbouring modes in a similar manner to lateral inhibition in retinal ganglion cells. Different lasing modes win the competition process when specific image features are present, providing feature detection by increasing their lasing amplitude - akin to the increased neuronal activity providing retinal feature detection. We integrate convolutional feature detection and strong physical nonlinearity in a single compact 150  $\mu\text{m}$  physical system, with ten image features detected in parallel by different lasing modes.

For image classification, detected feature maps are then re-illuminated onto the network to provide a subsequent classification layer with further physical nonlinear processing. A single logistic regression step is applied to the spectral output of this second layer, linearly multiplying each spectral channel by a single fixed weight to provide classification results. Accuracy scores of 98.05% and 87.85% are reported for MNIST digits and Fashion MNIST image classification tasks respectively. Strong classification performance is observed where the system is trained on small datasets, attractive for in-the-field learning applications such as edge-computing. The photonic system outperforms multiple software neural network architectures including CNNs and multilayer perceptrons for training sets below 5,000 (MNIST digits) and 10,000 (Fashion-MNIST) images. Close correlation is found between experimental results and theoretical modelling, highlighting nonlinear mode-competition between overlapping modes as the underlying physical mechanism responsible for feature detection.

## Results and Discussion

### Working Principle

The physical system employed here is a 150  $\mu\text{m}$  diameter InP network laser comprising interconnected lateral nanoscale waveguides, lithographically-patterned on a Si chip<sup>28,29</sup>. The network design is a random Voronoi topology with three waveguides meeting at each vertex (average waveguide length = 5  $\mu\text{m}$ ). A pump beam, spatially-structured by a digital

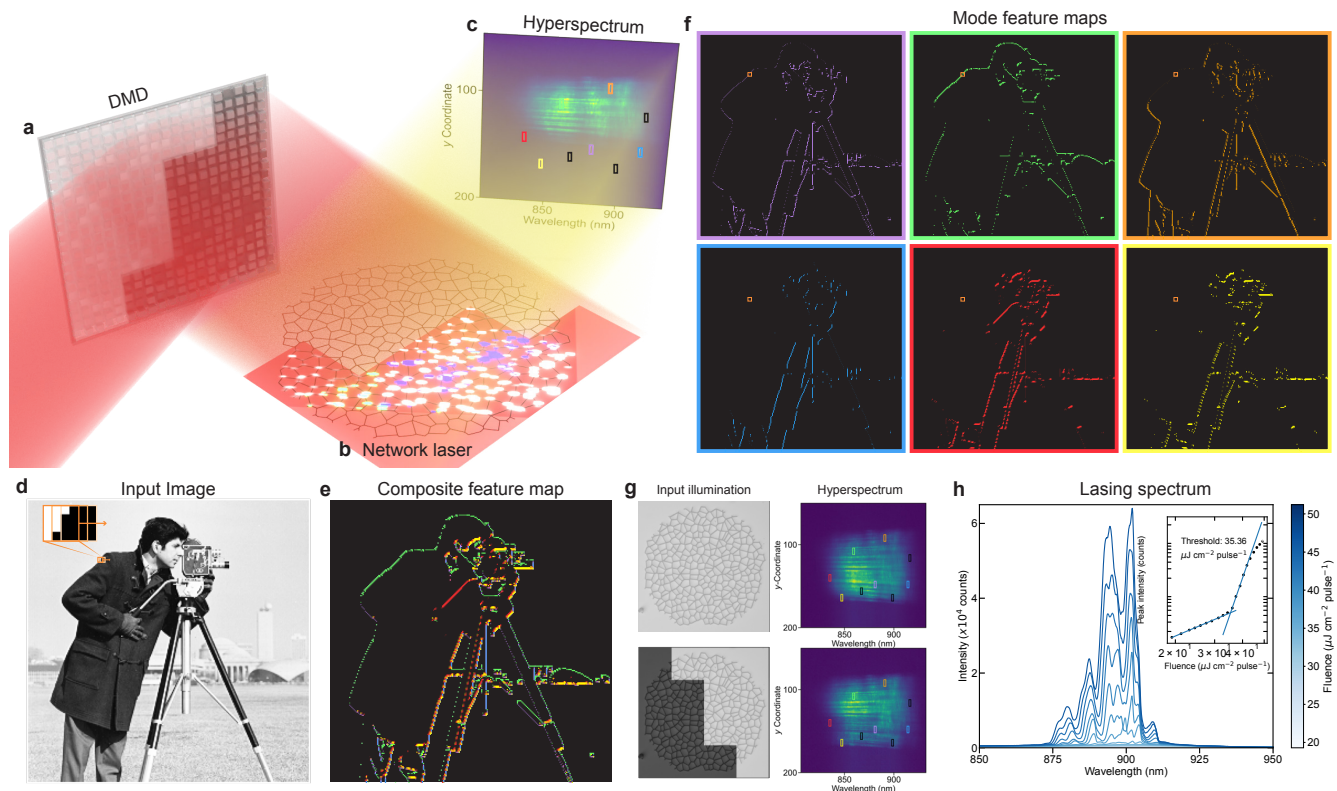


**Figure 1. Image feature detection in a complex network laser.**

- a)** Digital micromirror device takes 633 nm pump light and spatially structures it to an arbitrary input image.
- b)** Input image is illuminated onto 150  $\mu\text{m}$  InP network, triggering optical gain in the illuminated InP regions (highlighted in deeper red) and exciting photons which scatter through the network to produce many lasing modes at different wavelengths determined by the scattering paths. Spatial mode profiles of three lasing modes are indicated via different coloured nodes.
- c)** Lasing spectra emitted by the network are recorded via spatially-resolved spectrometer, giving ‘hyperspectral’ data with spectra recorded for one-dimensional slices across the network with approximately 1  $\mu\text{m}$  width. Modes detecting image features are highlighted by coloured boxes, corresponding to the feature maps in e) and f).
- d)** Input image is fractured into  $N \times N$  pixel windows (here  $4 \times 4$ ) and sequentially illuminated on the InP network as a raster scan. Small window on the person’s arm corresponds to the image illuminated in a-c).
- e)** Feature maps are produced by plotting the lasing amplitude of different modes. Each colour in the composite feature map corresponds to the lasing amplitude of a different mode, with 6 modes used to build this composite map.
- f)** Feature maps are shown for 6 separate modes, highlighting the range of image features detected in parallel by the system.
- g)** Examples of how different spatial illumination patterns produce different hyperspectral output. Coloured boxes indicate location of 10 feature-detecting modes.
- h)** Lasing spectra recorded under full illumination at different pump fluence. Lasing threshold behaviour is shown in inset.

micromirror device (DMD) (figure 1a), induces optical gain in the InP network (figure 1b). Photons are created by spontaneous emission and scatter through the network of waveguides, amplified by stimulated emission from the illuminated InP. Constructive interference along specific scattering paths defines the optical modes, which undergo net gain or loss depending on the extent of overlap between the illumination pattern and the mode profiles.

The large number of possible scattering paths results in many spatially-distributed overlapping modes which nonlinearly compete for gain. Pump illumination is supplied by a 633 nm, 200 fs pulse laser with 1 kHz repetition rate, with pulse energy measured at 43 nJ at the sample. The spatial distribution of light emitted from the network by three different modes are highlighted by the coloured nodes in figure 1b), with the data experimentally imaged by a frequency-resolved slit-scan camera. Fabrication and optical setup details are provided in the Methods and supplementary figure S1.

The system is capable of detecting multiple image features in parallel by illuminating small ‘windows’ of an input image in a raster-scan fashion, shown schematically in figure 1. Input image windows are illuminated on the network sequentially via a pump beam and DMD (fig. 1a,b), with varying network lasing spectra produced in response to different input images. The lasing response of the InP network is dispersed by a diffraction grating and projected onto a two-dimensional CCD detector.

This allows collection of ‘hyperspectra’ that are spatially resolved in one dimension (figure 1c), with separate lasing spectra recorded per  $\sim 1\mu\text{m}$  wide cross-sectional slice of the network.

Image feature maps are extracted by recording the amplitude of different modes as small ‘windows’ of an input image are scanned across the InP network (fig. 1d), here  $4\times 4$  pixel windows. Modes effectively provide functionality akin to convolutional filters, with lasing intensity increased or suppressed by the presence of different image features due to a combination of correlation between the input image shape and spatial mode profile, and nonlinear mode competition between spatially-overlapping modes. Specific modes lase strongly when a given image feature is present (e.g. a left or right hand edge), providing direct feature detection via the recorded spectrum. Examples of spectral output and mode intensities varying in response to different input images are shown in supplementary figure S2.

For a single input illumination, all modes undergo their lasing processes in parallel and multiple feature maps are obtained by plotting the lasing amplitude of selected modes at each position of the convolutional scan. A composite feature map comprising the lasing output of six modes is shown in figure 1e). The different colours on the composite map correspond to features detected by different spectral regions, indicated by boxes on figure 1c) (additional details in supplementary figure S2. Figure 1f) shows the six separate feature maps used to compose the composite map. As the modes providing the different feature maps overlap spatially within the same compact physical network, the scheme provides a space-efficient platform for parallel feature detection.

### Spectrally-multiplexed feature-detection

We can use physical modelling to examine the origin and functionality of the photonic feature-detection. Here, we employ a numerical model netSALT<sup>24</sup> which solves the nonlinear interaction of optical waves on graph networks within the steady-state ab-initio laser theory (SALT)<sup>30</sup> approximation. The netSALT model includes amplification and loss on graph edges and nonlinear competition between spatially-overlapping lasing modes. Figure 2a) shows a random Voronoi graph network used for the netSALT simulations. Network topology and average edge length ( $5\mu\text{m}$ ) match the experimentally measured network shown in fig. 1, with a smaller  $50\mu\text{m}$  diameter used in simulation to reduce computational load.

Three illumination patterns are explored: uniform illumination (‘full’), horizontal edge (‘right’) and vertical edge (‘top’) (fig. 2b). The resultant simulated netSALT lasing spectra are shown for the three illuminations in figure 2c), showing strong variation in lasing spectra under the different illumination patterns.

NetSALT predicts 239 possible lasing modes for the network considered here, with 172 attaining lasing threshold for at least one of the illumination patterns. The three spectra in fig. 2c) show the sum of all active modes for the different illumination patterns. To gain a better understanding of the behaviour of specific modes which drive the feature-detection process, we examine three specific modes, labelled A,B,C, identified in figure 2c) by dashed vertical lines. Figure 2d) shows the lasing amplitude of the three modes under ‘full’, ‘right’ and ‘top’ illumination patterns with the spatial mode profiles inset in the left-hand panel. The modes are spatially-distributed across the network, with non-zero spatial overlap between the three modes. As multiple modes are active in the same regions of the network, nonlinear mode-competition occurs between the modes as they antagonistically compete for gain. Under full illumination, mode B shows the highest amplitude, while mode C does not lase at all as it falls below the lasing threshold. For a right-edge illumination mode B now falls below the lasing threshold and is deactivated, allowing mode C to lase with the highest amplitude as it no longer faces strong mode-competition from the mode B. For a top-edge illumination, mode A exhibits far higher amplitude and mode C now falls below the lasing threshold.

It is important to note that modes A and C exhibit higher lasing amplitude under ‘top’ and ‘right’ edge illuminations, where the network receives less input pump energy than under uniform illumination. This is not possible in a linear system with non-interacting modes, and occurs here as removing pump light from some network regions causes modes residing even partially in those regions to lose the mode-competition interactions, e.g. mode B winning under full illumination and losing under edge illumination. This observed behaviour shows that nonlinear competition for gain between spatially-overlapping modes is providing feature-sensitive lasing dynamics, analogous to the lateral inhibition processes in retinal ganglion cells.

We now consider the netSALT-simulated feature-detection performance of the system. An input image of the letters CL (complex lasing) is shown in fig. 2e). The image was fractured into  $8\times 8$  pixel windows and illuminated on the network in a raster-scan fashion. The lasing response was simulated for each window illumination, and the mode lasing amplitude plotted at each position in the raster scan to generate separate feature-maps for each mode.

Figure 2f) shows feature maps provided by five different modes, with the corresponding spatial mode profiles inset. These plots demonstrate the ability of the network to perform spectrally-multiplexed feature-detection of a range of image features, with the broad set of lasing modes effectively providing parallel convolutional filters. The spatial location of the mode profiles within the network are seen to show correspondence with the detected image features, e.g. modes detecting lower image edges are located towards the bottom of the network, modes detecting left edges are located towards the left of the network, and so on. Of the 172 active modes in the simulated network, 40 were identified as exhibiting good feature-detection. A set of 28 selected feature maps and corresponding spatial mode profiles is shown in the supplementary figure S3, alongside the full set of 172



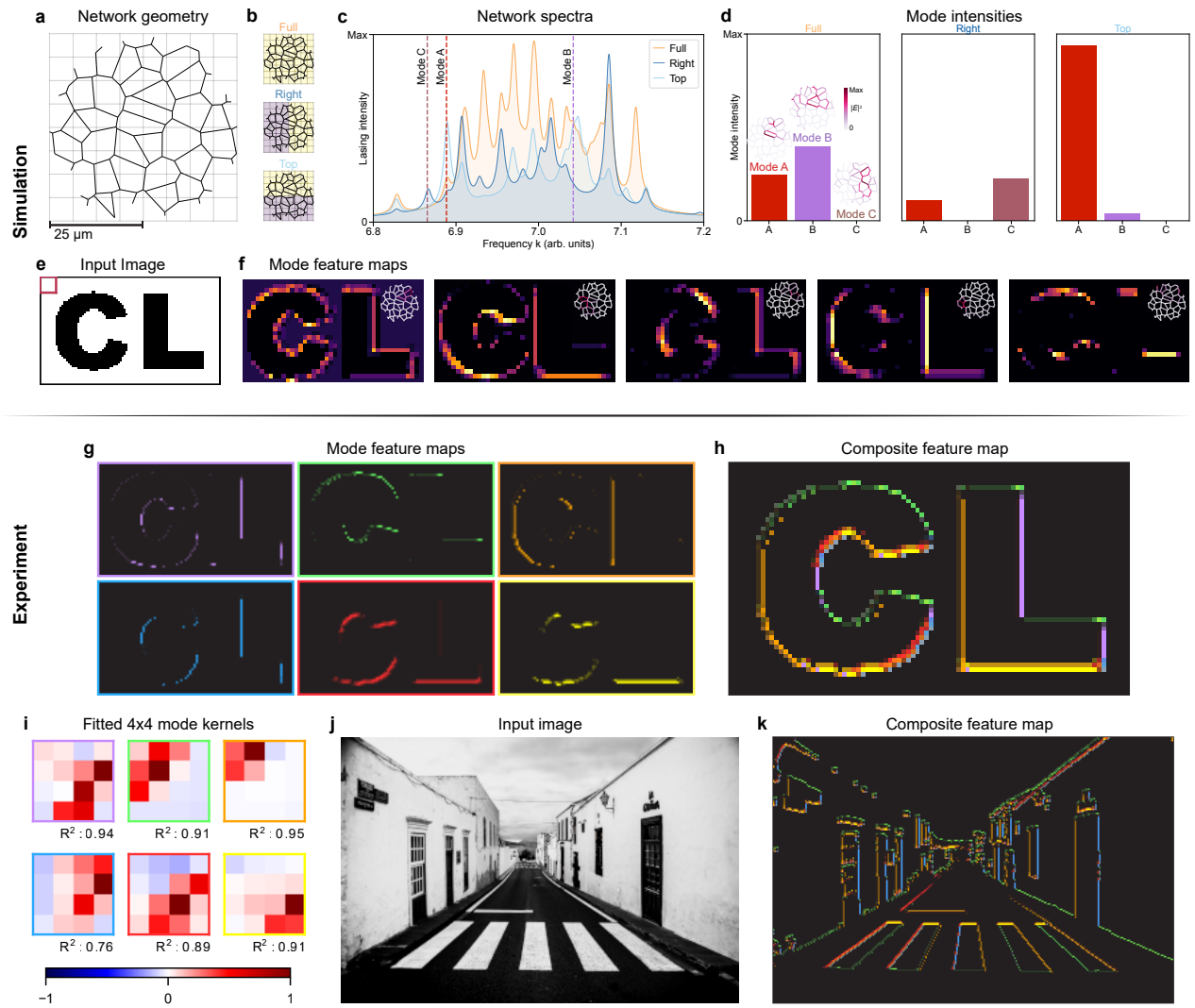


**Figure 2. Parallel image feature-detection via network lasing modes.** a-f) are simulation results, g-k) are experimental. **a)** 50  $\mu\text{m}$  network topology used for netSALT simulations a-f). **b)** Three network illumination patterns: uniform, horizontal edge and vertical edge. **c)** Simulated network lasing spectra for the three illumination patterns. Three modes A-C are indicated, corresponding to d). **d)** Simulated lasing mode intensities of three modes A-C for the three network illumination patterns. Mode competition nonlinearly suppresses different modes below lasing threshold and amplifies other modes dependent on input image. Spatial mode profiles are shown inset in the left panel. **e)** Input image, ‘CL’ for ‘complex lasing’. The input image is fractured into  $8 \times 8$  pixel windows and illuminated onto the network sequentially in a raster-scan fashion, similar to kernel scanning in a convolutional filter process. **f)** Simulated feature maps for five modes. Pixel brightness in the feature maps corresponds to the mode lasing intensity for that position in the window raster-scan. Different lasing modes respond to different image features, spatial mode profiles are shown inset. A larger set of 28 simulated feature maps corresponding to different image features, is shown in the supplementary information. **g)** Experimentally recorded ‘CL’ feature maps produced from six modes. As in simulation, different lasing modes respond to different image features. **h)** Experimental composite feature map comprising modes from g). **i)** Equivalent  $4 \times 4$  kernels for the six lasing modes, extracted by fitting experimental data. Coloured frames correspond to mode feature map colour scheme.  $R^2$  scores suggest the effective linear kernels fail to capture some of the nonlinear physical dynamics. **j)** Photographic test image of a street scene,  $300 \times 200$  pixel resolution. input image. **k)** Experimental composite feature map of the street test image.

feature maps from all modes in supplementary figure S4. A regular hexagonal network was simulated to compare with the random graph topology with far fewer detected features, shown in supplementary figure S5.

We now examine experimental feature detection. Figure 2g) shows six experimentally measured feature maps of the ‘CL’ image with colours corresponding to the modes shown in figure 1 and a composite feature map shown in figure 2h). Parallel feature detection of multiple image features is observed experimentally, with close correspondence to the netSALT simulated behaviour. Supplementary figures S6, S7 and S8 examine the feature detection performed by ten lasing modes across a range of

test images. To compare our physically-detected feature maps against linear matrix kernel filters as used in software CNNs, we extract effective kernel filters for our modes via least-squares fitting between input images and the experimentally measured mode intensity (details in supplementary information). The extracted effective filters are shown in fig. 2i) with further details in supplementary fig. S9. Notably, both positive and negative kernel weights are observed - generating bipolar weights is highly challenging in neuromorphic hardware and an attractive benefit of the photonic lateral inhibition processes in our system which enable mode amplitude to both increase and decrease in response to specific image features. The  $R^2$  values below each effective kernel indicate how well the linear fitting process captures our experimental results. When performing the same kernel fitting process on arbitrary linear software kernel filters, the process performs perfectly with  $R^2$  values of 1.0. The kernels extracted from our experimental data have  $R^2$  values from 0.628-0.946 (see fig. S9), suggesting that aspects of the physical feature detection process cannot be fully captured by linear kernel filters.

The experimental feature detection capability is proven for a higher-resolution ( $300 \times 200$  pixel) photographic image of a street scene, shown in figures 2j,k). Separate lasing mode feature maps are shown for all test images in supplementary figures S10, S11 and S12.

### Multi-layer convolutional image classification

The feature maps detected by the network can be leveraged for machine vision tasks such as image classification, effectively providing an initial convolutional processing layer. Here we demonstrate the ability of the system to classify images, benchmarking classification via the MNIST digits and Fashion-MNIST tasks. For each task, we experimentally process 40,000 training images with a test set of 4000 images and training sets of 125 to 36,000 images.

For image classification we employ a multi-layer architecture, depicted schematically in figure 3a-c): an initial convolutional layer which performs feature detection as described above (fig. 3a), then a second layer where the detected feature maps are illuminated on the network as a single whole image (fig. 3b) with a logistic regression step applied to the spectral output of the second layer to generate classification results (fig. 3c).

Ten spectral regions performing feature detection were selected, producing ten feature maps per input image. Three feature maps are shown schematically in figure 3b), with all feature maps for a range of MNIST digits and Fashion-MNIST shown in supplementary figures S13 and S14. These feature maps are then re-illuminated on the InP network as whole images, illustrated in the experimental camera image in figure 3b). The hyperspectral output from the second-layer feature map illuminations are combined in parallel and a single logistic regression step is applied in software to produce classification results. The same approach is employed for both MNIST digits (fig. 3a-c) and Fashion-MNIST (fig. 3d,e) tasks. We achieve an accuracy of 98.05% and 87.85% for MNIST digits and Fashion-MNIST respectively, further details of the regression process including feature selection are given in the Methods.

As a control, we perform the same final software logistic regression step directly on the input image data, bypassing the optical system. Substantially lower accuracies are observed of 92.10% and 82.29% for the MNIST digits and Fashion-MNIST tasks respectively.

Beyond comparisons against logistic regression, figures 3f,g) show a comparison of classification accuracy vs. training dataset length for a range of software neural networks. Five approaches are compared: the photonic network, software logistic regression, a software multi-layer perceptron, and two software CNNs: one following the LeNet5 architecture, and a larger CNN with more filters and neurons. Full details of the comparison networks are provided in the methods. Training dataset length is varied from 125 to 36,000 images, with a fixed 4000 image test set. We also benchmarking against quasi-isomorphic software networks, comprising an initial convolutional filter layer of  $10 \times 4 \times 4$  filters followed by 30,000 randomly weighted ReLu neurons and a final logistic regression layer to mirror the structure of the experimental system. The results are shown in the supplementary information for two cases, one with random kernel filter weights and one using the kernel filter weights fitted from experimental data as shown in figure 2i).

At shorter training set lengths, the photonic network achieves higher accuracy than the software benchmarks. The photonic network scores highest for training sets below 5000 (digits) and 15,000 (fashion) images, demonstrating the learning strengths of the photonic system when working with short training datasets.

As one of the key proposed applications for neuromorphic computing hardware is ‘edge computing’ where remotely deployed hardware performs computation directly at the point of sensing, it is highly advantageous to perform well with short training sets. As edge-computing applications often demand that a system is able to adapt on-the-fly to changing environmental conditions and perform computation on remotely collected data without access to large offline training sets, the ability to perform well on short training sets is a strong benefit of this system.

## Conclusions

We have demonstrated a photonic machine vision platform based on a network laser. The system is capable of performing parallel feature detection, nonlinear activation and image classification in a single  $150 \mu\text{m}$  on-chip InP network with encouraging

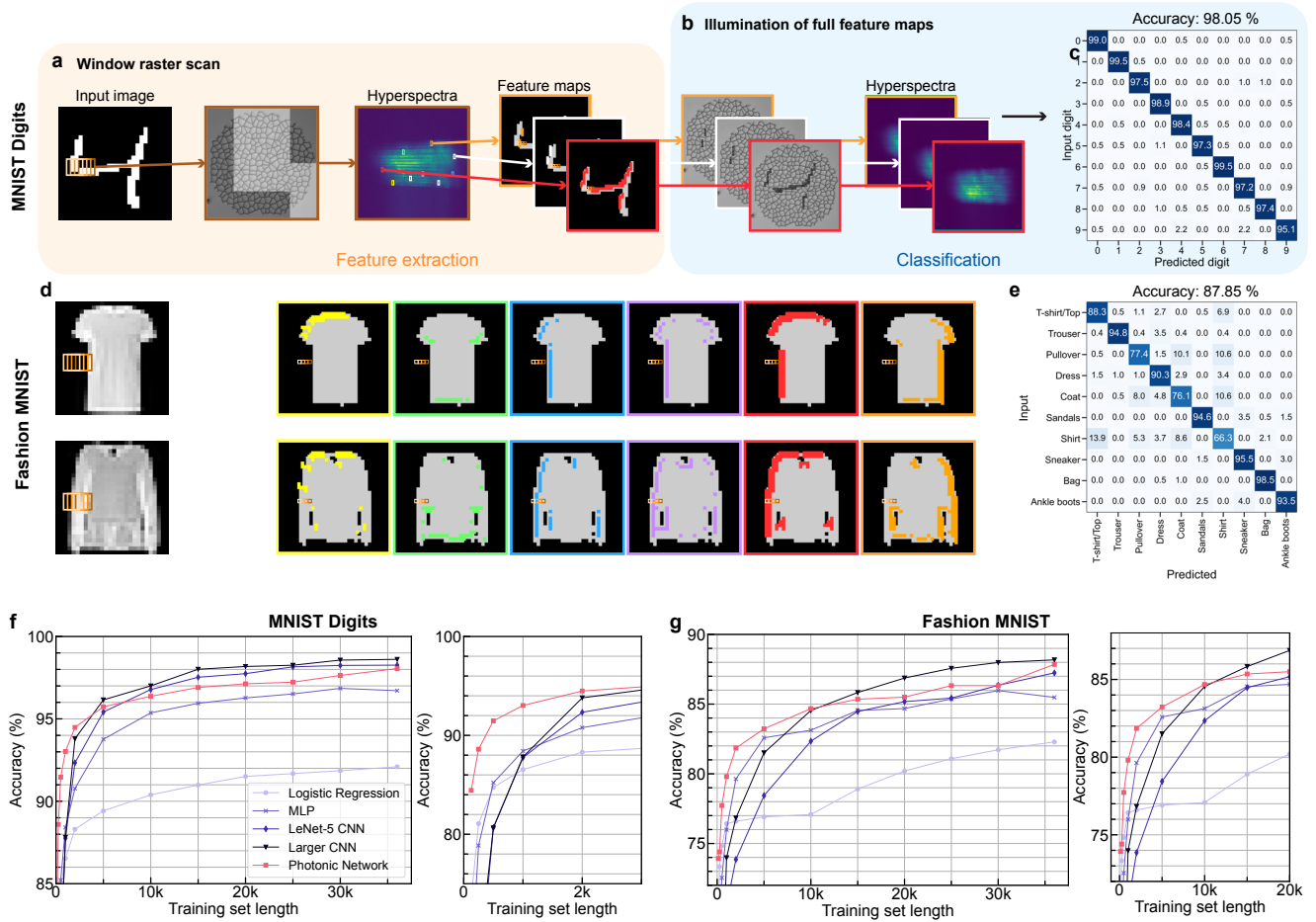


**Figure 3. Multilayer image classification.**

**a)** Feature detection: Input images are fractured into 4x4 pixel windows which are illuminated on the InP network in a sequential raster scan. The lasing amplitude of ten selected modes are used to perform spectrally-multiplexed feature detection and generate ten feature maps (three shown here, all ten shown in SI).

**b)** Classification: Detected feature maps are then illuminated onto the network as whole images in a single illumination step with no window scanning. Output spectra are recorded for each feature map, giving ten spectra per image.

**c)** The ten spectra are then combined in parallel, and a single logistic regression step is applied during training to generate a set of weights, one per hyperspectral channel (36813 channels after feature selection for MNIST-digits). For testing, no further regression is applied - each hyperspectral channel is multiplied by the fixed weights for each class obtained during training then summed. The class receiving the highest sum is then given as the prediction. A test accuracy of 98.05% is achieved for MNIST-digits.

**d)** The same architecture is employed for the Fashion-MNIST task. Two input images are shown with six feature maps, colours corresponding to the modes shown in figures 1 and 2.

**e)** A test accuracy of 87.85% is achieved for Fashion-MNIST.

**f,g)** Training length vs. test classification accuracy comparison for MNIST digits (f) and Fashion-MNIST (g), with a zoomed-in plot of classification performance at shorter training sets for each task. The photonic convolutional network is compared against four software approaches: Logistic regression performed on the raw image data, a multi-layer perceptron, a LeNet-5 software CNN and a larger CNN (network details in text).

classification results, particularly on short datasets.

As the lasing modes responsible for feature detection spatially overlap, within the same InP network we are able to provide compact feature detection of multiple image features. In contrast, existing physical convolutional hardware schemes typically detect one feature per repeat of the device, hence the spatial footprint, fabrication complexity and energy consumption typically scale with the number of features detected. While we currently experimentally detect ten parallel image features, we find up to forty in simulation and the number of detected features is likely to increase as we deepen understanding of the links between network topology and feature sensitivity.

A key result of this work is demonstrating the importance of including both excitatory and inhibitory interactions in neuromorphic hardware. In biological systems, both of these interactions and their interplay are crucial to providing neuronal functionality<sup>14,15,17</sup>, and existing physical neuromorphic hardware platforms often focus on excitatory signals. By engineering inhibitory nonlinear mode-competition between network lasing modes, we demonstrate the functional benefits of bio-inspired inhibitory dynamics.

As we develop finer control over the network dynamics, one can envision networks engineered to detect arbitrary specific features or provide reconfigurable detection via altering network dynamics via electrical gating or selective illumination of network sub-regions. More broadly, our approach shows the benefits of designing photonic computing systems with intrinsic physical nonlinearities and a dynamic balance of competing excitatory and inhibitory interactions.

### Author contributions

RS, JCG, KM and KS conceived the work.

RS, KM, JCG, KS and WRB secured funding.

WKN, JD, DS, TF and AF performed optical experiments.

JCG and KS designed the neuromorphic computing architecture.

RS, KM, HS, AF, DS and JD designed and developed the network laser concept.

JD, KM and HS fabricated the InP network.

TVR performed all simulations.

JCG, KS and TF performed machine learning analysis.

JD and TS performed analysis of experimental feature-detection functionality.

MB provided guidance on physical simulations using the netSALT code and guidance on implementing the machine learning architecture.

JP designed a benchmarking task used to develop the computing architecture.

AF designed and produced the figures with contributions from JD.

JCG wrote the manuscript with contributions from all authors.

### Acknowledgements

This work was supported by the Royal Academy of Engineering Research Fellowships, awarded to JCG.

JCG was supported by the EPSRC ECR International Collaboration Grant EP/Y003276/1.

AF, JD, HM, RS and KM acknowledge support from the EU ITN EID project CORAL (GA no. 859841).

TVR, DS, and RS acknowledge support from The Engineering and Physical Sciences Research Council (EPSRC), grant number EP/T027258.

WKN acknowledges the research support funded by the President's PhD Scholarships from Imperial College London.

This work was supported by the EPSRC Impact Acceleration Account fund awarded to JCG and RS.

This work was supported by the Imperial College London DT-Prime scheme awarded to JCG, RS and MB.

KDS was supported by The Eric and Wendy Schmidt Fellowship Program and the Engineering and Physical Sciences Research Council (Grant No. EP/W524335/1).

TF was supported by the EPSRC doctoral training programme PhD award.

JP performed the work as part of his Physics MSci project at Imperial College London.

The InP network laser samples were fabricated in the Binnig and Rohrer Nanotechnology Center (BRNC) at IBM Research Europe - Zurich. We thank Markus Scherrer, Daniele Caimi and the Cleanroom Operations Team of the BRNC for their help and support.

We thank David Mack for excellent laboratory management and Steve Cussell and Dave Bowler for excellent technical workshop services at Imperial College London.

We thank Christine Zhao and Eunju Moon for their helpful discussions and contributions to the project.

Simulations were performed on the Imperial College London Research Computing Service<sup>31</sup>.

Test image of 'cameraman' was used with CC BY-NC 4.0 creative commons licence, first appearance in Schreiber et al<sup>32</sup>. Obtained from [dome.mit.edu/handle/1721.3/195767](https://dome.mit.edu/handle/1721.3/195767).

Test image of 'street scene' was used with CC0 1.0 universal creative commons licence, photographer Christian Birkholz, taken



2013. Obtained from pixabay.com/photos/calle-jose-betancort-teguise-201343/.  
Test image of 'CL' letters was generated by the authors.

### Competing interests

The authors declare no competing interests.

### Data availability statement

The datasets generated during and/or analysed during the current study are available from the corresponding author on reasonable request.

### Code availability statement

The code used in this study is available from the corresponding author on reasonable request.

## Methods

### Experimental methods

#### Fabrication

The InP networks are fabricated on a Si chip with a 2  $\mu\text{m}$  buffer layer of  $\text{SiO}_2$  (SOI chip) according to<sup>29</sup>. To obtain a defect-free InP layer on SOI, we used a Direct Wafer Bonding approach where the 127 nm thick InP layer is grown on a sacrificial III-V semiconductor wafer, with lattice-constant matched growth. This wafer is then annealed onto the SOI wafer and the sacrificial wafer removed by wet etching, resulting in a InP on SOI wafer that is cleaved into chips. The network structures are then patterned into a spin-coated hydrogen silsesquioxane (HSQ) mask with electron beam lithography. The pattern is transferred into the InP layer using Inductively Coupled Plasma (ICP) Reactive Ion Etching (RIE)<sup>29</sup> using a cyclic two-stage process: a  $\text{CH}_4$  and  $\text{H}_2$  plasma stage for etching, followed by  $\text{O}_2$  plasma stage for cleaning. To reduce surface state recombination losses and oxidation, the structures are passivated with phosphoric acid and coated with 3 nm of  $\text{Al}_2\text{O}_3$  using Atomic Layer Deposition (ALD)<sup>33</sup>.

#### Network design

The network was designed by using a random point pattern on a plane and generating a Voronoi diagram<sup>28</sup>. The network is cropped to a circular area with 150  $\mu\text{m}$  diameter, and the density of the point patterns is varied to generate waveguide graph-edges with 350 nm width and an average length of 5  $\mu\text{m}$ .

#### Optical setup

The edge-detection and digit classification experiments are performed in an optical microscopy setup with a spatially-structured pump (via DMD) to excite the network laser structure. A schematic of the setup is shown in the supplementary information, fig. S1). The pump laser of a 633 nm femtosecond pulsed laser (Light Conversion PHAROS with ORPHEUS-VIS Optical Parametric Amplifier (OPA) and LYRA harmonic generator, 200 fs pulse duration, 1 kHz repetition rate) is first expanded through a telescope and shaped by reflecting on a digital micromirror device (DMD, ViALUX V-650L). The DMD consist of  $1280 \times 800$  programmable mirror pixels which shape the incident uniform beam into any pixelated black-and-white image (i.e. training images). The power of the shaped pump patterns is modulated by a motorised continuously variable neutral density (ND) filter, and the exact power received on the sample is monitored by a power meter (Thorlabs, S120VC Si photodiode, 200 - 1100 nm) on the split path reflected from a glass slide inserted. The spatially-structured pump is focused on the sample through a  $20\times$  objective (Olympus Plan N 20x with a 0.4 numerical aperture (NA)). The lasing emission from the network is collected through the same objective, filtered (Thorlabs FELH0750, 750 nm long-pass filter), and spatially and spectrally analysed using a grating spectrometer (Princeton Instruments SpectraPro HRS-300) equipped with a 600 g/mm visible grating without an entrance slit. The signals are measured by a 2D charge-coupled device camera (CCD, Princeton Instruments Pixis 256) with a spatial resolution of  $\sim 1\mu\text{m}$ .

#### Hyperspectral measurements

The raw hyperspectral data recorded by the CCD has 1024 spectral channels and 256 spatial channels. For feature detection, hyperspectral regions comprising four adjacent spectral channels and eight adjacent spatial channels are used to generate each feature map, with the averaged intensity taken within the hyperspectral region.

For the image classification layer, the hyperspectra are divided into averaged regions of sixteen adjacent spectral channels and four adjacent spatial channels, with each region passed to the logistic regression layer and assigned a single fixed linear weight during training.

The region-selection and averaging performed here could be implemented by using a lower resolution spectrometer, with the additional benefits of faster data acquisition and lower cost.

### NetSALT simulations

The lasing modes and intensities of the network are modelled using netSALT<sup>24</sup>. The designed network is represented as a graph, with the edges subdivided to overlap with an 8x8 grid to correspond to the kernel. When the network is unpumped, each edge has a complex refractive index  $n = 3.4 + 0.001i$ . The edges are further assumed to have a Lorentzian gain profile centered at normalised frequency  $k_a = 7$  with a width  $\gamma_a = 0.35$ , and are pumped up to a normalised power  $D_0 = 0.5$  (For a detailed physical explanation of the parameters, see Ref. 24). A separate simulation is performed for each 8x8 binary kernel, by pumping only the edges falling under the illuminated pixels. The passive (without pumping) modes of the network are first identified in the complex frequency plane  $k$ , and these are the same for all kernels. For each kernel, the modes are tracked in the complex plane as the pump power is increased, allowing to compare between the same modes across different kernels. As a mode reaches the real frequency plane [ $\text{Im}(k) = 0$ ], it attains threshold and starts lasing. Beyond this pump power, the frequency and shape of the mode do not change but mode competition between the lasing modes modifies their lasing intensities. They further deplete the gain available to the remaining modes, increasing their thresholds. The mode frequencies, thresholds and intensities found by netSALT incorporate the mode competition, gain depletion and nonlinearity.

As netSALT provides one mode frequencies and intensities but not the widths, the realistic spectra in Fig. 2c are created by assigning a width of 0.005 to each mode and adding a broad photoluminescence background. The mode feature maps in Fig. 2f are made by selecting specific modes and plotting their intensities for the kernels corresponding to the kernel scan of Fig. 2e.

### Regression process for the network laser image classification task

Hyperspectra are recorded for the ten feature-maps for each of the 40,000 input images, with initial hyperspectral resolution of 1024 spectral channels and 256 spatial channels. The top and bottom 25 spatial channels are discarded as they fall outside the InP network, leaving 206 spatial channels.

These channels are then binned using simple averaging with binning factors of 16 and 2 for the spectral and spatial channels to give 64 and 103 spectral and spatial channels respectively per feature map.

The spectral and spatial channels of all feature maps are then combined in parallel to produce a single 2D array, with each row of the array corresponding to a single input image and each column corresponding to a single ‘pixel’ of the binned hyperspectra.

The array is separated into separate ‘train’ and ‘test’ sections, with final accuracy results of 98.05% (MNIST-digits) and 87.85% (Fashion-MNIST) reported from train and test lengths of 36,000 and 4000 images respectively.

Feature selection is performed on the data using the SelectKBest function from Sklearn, using Chi-squared correlation between the hyperspectral data and the ground-truth image class labels in the training set. A parameter search was performed to identify 36,000 as the number of features to keep from the initial pool of 58,000 features.

After feature selection, logistic regression is performed on the training data using sklearn’s logisticRegression function. The lbfgs solver was used with a regularisation parameter of  $C = 6.8$ , identified using a parameter search.

### Software machine learning comparisons for image classification

We benchmark our system against four software approaches for the MNIST and Fashion-MNIST tasks: logistic regression, a multi-layer perceptron and a convolutional neural network (LeNet5) and a larger convolutional neural network model with many more filters and trainable parameters.

The model descriptions and number of trainable parameters for each model are given below, models were coded in python using the sklearn, keras and pytorch packages.

#### Multi-layer Perceptron

The multi-layer perceptron comprises an input layer of 784 neurons (one per 28x28 image pixel), an initial hidden layer of 300 neurons with ReLU nonlinear activation, a second hidden layer of 100 neurons with ReLU nonlinear activation, and then a final softmax layer.

- **Input Layer:**
  - Neurons: 784 (one per 28x28 image pixel)

- **Hidden Layer 1:**
  - Neurons: 300
  - Activation: ReLU (Rectified Linear Unit)
- **Hidden Layer 2:**
  - Neurons: 100
  - Activation: ReLU
- **Output Layer:**
  - Neurons: 10
  - Activation: Softmax

**Number of Trainable Parameters:**

Input Layer to Hidden Layer 1:  $(784 + 1) \times 300 = 235,500$  parameters  
 Hidden Layer 1 to Hidden Layer 2:  $(300 + 1) \times 100 = 30,100$  parameters  
 Hidden Layer 2 to Output Layer:  $(100 + 1) \times 10 = 1,010$  parameters  
**Total Trainable Parameters:**  $235,500 + 30,100 + 1,010 = 266,610$  parameters

**LeNet-5 CNN Structure:**

The LeNet-5 convolutional neural network architecture comprises seven layers: two convolutional layers each followed by a max pooling layer, two fully connected layers then a final softmax output layer. In total, 22 convolutional filters are used.

- Convolutional Layer 1:
  - Filters: 6
  - Kernel Size:  $5 \times 5$
  - Activation: ReLU
  - Input Shape:  $28 \times 28 \times 1$
- Max Pooling Layer 1:
  - Pool Size:  $2 \times 2$
  - Strides:  $2 \times 2$
- Convolutional Layer 2:
  - Filters: 16
  - Kernel Size:  $5 \times 5$
  - Activation: ReLU
- Max Pooling Layer 2:
  - Pool Size:  $2 \times 2$
  - Strides:  $2 \times 2$
- Flatten Layer
- Fully Connected Layer 1:
  - Neurons: 120
  - Activation: ReLU
- Fully Connected Layer 2:
  - Neurons: 84
  - Activation: ReLU
- Output Layer:
  - Neurons: 10
  - Activation: Softmax

### Number of Trainable Parameters:

Convolutional Layer 1:  $(5 \times 5 + 1) \times 6 = 156$  parameters per filter

Total for 6 filters:  $5 \times 156 = 780$  parameters

Convolutional Layer 2:  $(5 \times 5 \times 6 + 1) \times 16 = 2,416$  parameters per filter

Total for 16 filters:  $2 \times 2,416 = 4,832$  parameters

Fully Connected Layer 1:  $(5 \times 5 \times 16 + 1) \times 120 = 48,120$  parameters

Fully Connected Layer 2:  $(120 + 1) \times 84 = 10,164$  parameters

Output Layer:  $(84 + 1) \times 10 = 850$  parameters

**Total Trainable Parameters:**  $780 + 4,832 + 48,120 + 10,164 + 850 = 64,746$  parameters

### Larger CNN model

The larger CNN model has a more complex structure than the LeNet-5 CNN, with more kernel filters and trainable parameters. In total, 96 convolutional filters are used.

- Convolutional layer 1:
  - Input channels: 1
  - Number of filters: 32
  - Kernel size:  $3 \times 3$
- Max pooling layer 1:
  - Kernel size:  $2 \times 2$
- Convolutional layer 2:
  - Input feature maps: 32
  - Number of filters: 64
  - Kernel size:  $3 \times 3$
- Max pooling layer 2:
  - Kernel size:  $2 \times 2$
- Fully connected layer 1:
  - Input size:  $64 \times 5 \times 5 = 1600$
  - Output size: 128
- Fully connected layer 2:
  - Input size: 128
  - Output size: 10

### Number of Trainable Parameters

The number of trainable parameters in the model is calculated as follows:

Conv1 parameters =  $(1 \times 32 \times 3 \times 3) + 32 = 320$

Conv2 parameters =  $(32 \times 64 \times 3 \times 3) + 64 = 18,496$

FC1 parameters =  $(64 \times 5 \times 5 \times 128) + 128 = 204,928$

FC2 parameters =  $(128 \times 10) + 10 = 1,290$

**Total Trainable Parameters** =  $320 + 18,496 + 204,928 + 1,290 = 225,034$



## References

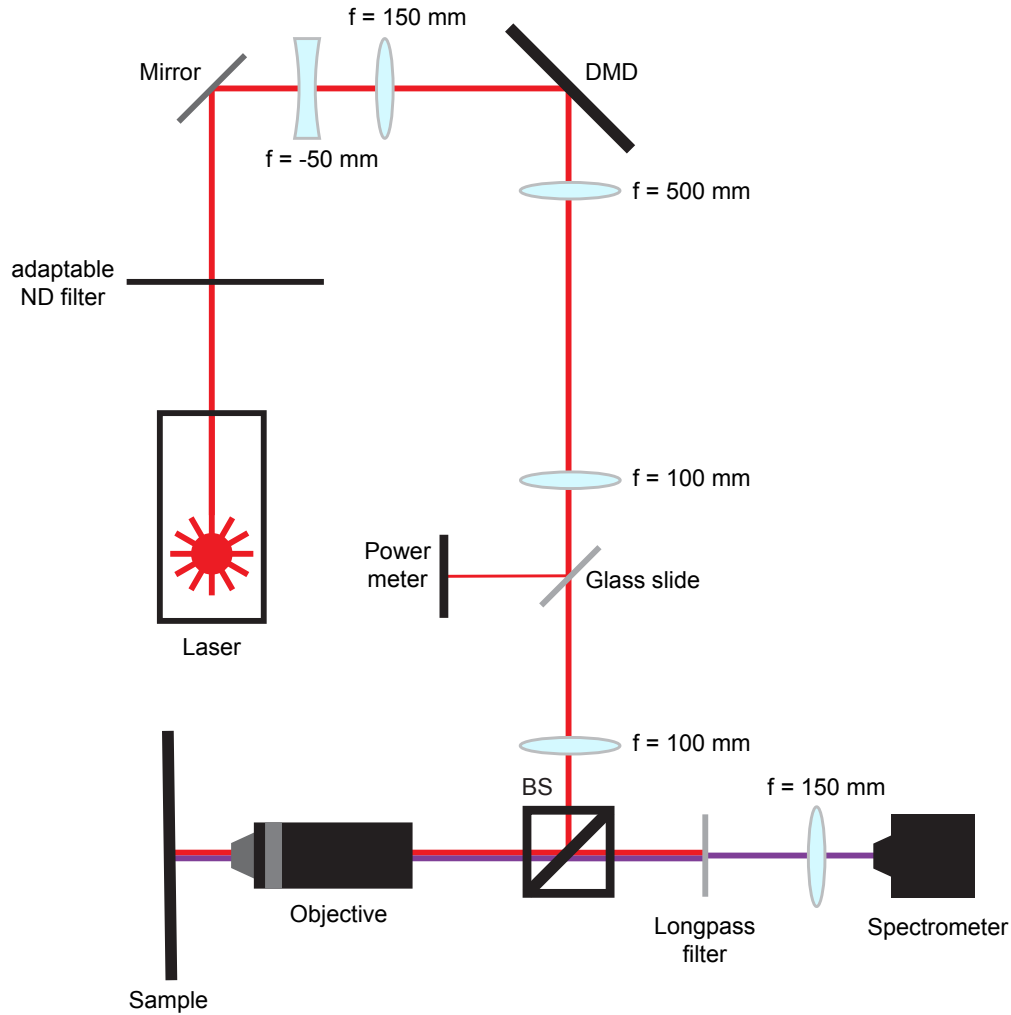
1. LeCun, Y. *et al.* Learning algorithms for classification: A comparison on handwritten digit recognition. *Neural networks: statistical mechanics perspective* **261**, 2 (1995).
2. O'shea, K. & Nash, R. An introduction to convolutional neural networks. *arXiv preprint arXiv:1511.08458* (2015).
3. Li, Z., Liu, F., Yang, W., Peng, S. & Zhou, J. A survey of convolutional neural networks: analysis, applications, and prospects. *IEEE transactions on neural networks learning systems* **33**, 6999–7019 (2021).
4. Gu, J. *et al.* Recent advances in convolutional neural networks. *Pattern recognition* **77**, 354–377 (2018).
5. Chellapilla, K., Puri, S. & Simard, P. High performance convolutional neural networks for document processing. In *Tenth international workshop on frontiers in handwriting recognition* (Suvisoft, 2006).
6. Alzubaidi, L. *et al.* Review of deep learning: concepts, cnn architectures, challenges, applications, future directions. *J. big Data* **8**, 1–74 (2021).
7. Yao, P. *et al.* Fully hardware-implemented memristor convolutional neural network. *Nature* **577**, 641–646 (2020).
8. Feldmann, J. *et al.* Parallel convolutional processing using an integrated photonic tensor core. *Nature* **589**, 52–58 (2021).
9. Xu, X. *et al.* 11 tops photonic convolutional accelerator for optical neural networks. *Nature* **589**, 44–51 (2021).
10. Zheng, H. *et al.* Multichannel meta-imagers for accelerating machine vision. *Nat. Nanotechnol.* 1–8 (2024).
11. Shastri, B. J. *et al.* Photonics for artificial intelligence and neuromorphic computing. *Nat. Photonics* **15**, 102–114 (2021).
12. Liao, K., Dai, T., Yan, Q., Hu, X. & Gong, Q. Integrated photonic neural networks: opportunities and challenges. *ACS Photonics* **10**, 2001–2010 (2023).
13. Farnakidis, N., Dong, B. & Bhaskaran, H. Integrated photonic neuromorphic computing: opportunities and challenges. *Nat. Rev. Electr. Eng.* 1–16 (2024).
14. Kerschensteiner, D. Feature detection by retinal ganglion cells. *Annu. review vision science* **8**, 135–169 (2022).
15. Fairhall, A. L. *et al.* Selectivity for multiple stimulus features in retinal ganglion cells. *J. neurophysiology* **96**, 2724–2738 (2006).
16. Masland, R. H. The neuronal organization of the retina. *Neuron* **76**, 266–280 (2012).
17. Thoreson, W. B. & Mangel, S. C. Lateral interactions in the outer retina. *Prog. retinal eye research* **31**, 407–441 (2012).
18. Werblin, F. S. The retinal hypercircuit: a repeating synaptic interactive motif underlying visual function. *The J. physiology* **589**, 3691–3702 (2011).
19. Marković, D., Mizrahi, A., Querlioz, D. & Grollier, J. Physics for neuromorphic computing. *Nat. Rev. Phys.* **2**, 499–510 (2020).
20. Cao, H., Chriki, R., Bittner, S., Friesem, A. A. & Davidson, N. Complex lasers with controllable coherence. *Nat. Rev. Phys.* **1**, 156–168 (2019).
21. Sapienza, R. Controlling random lasing action. *Nat. Phys.* **18**, 976–979 (2022).
22. Wiersma, D. S. The physics and applications of random lasers. *Nat. physics* **4**, 359–367 (2008).
23. Cerjan, A. *et al.* Controlling mode competition by tailoring the spatial pump distribution in a laser: a resonance-based approach. *Opt. Express* **24**, 26006–26015 (2016).
24. Saxena, D. *et al.* Sensitivity and spectral control of network lasers. *Nat. Commun.* **13**, 6493 (2022).
25. Van der Molen, K. L., Tjerkstra, R. W., Mosk, A. P. & Lagendijk, A. Spatial extent of random laser modes. *Phys. review letters* **98**, 143901 (2007).
26. Bachelard, N., Gigan, S., Noblin, X. & Sebbah, P. Adaptive pumping for spectral control of random lasers. *Nat. physics* **10**, 426–431 (2014).
27. Gaio, M. *et al.* A nanophotonic laser on a graph. *Nat. communications* **10**, 226 (2019).
28. Saxena, D. *et al.* Designed semiconductor network random lasers. *Submitted* (2024).
29. Dranczewski, J. *et al.* Plasma etching for fabrication of complex nanophotonic lasers from bonded InP semiconductor layers. *Micro Nano Eng.* **19**, 100196, DOI: [10.1016/j.mne.2023.100196](https://doi.org/10.1016/j.mne.2023.100196) (2023).
30. Ge, L., Chong, Y. D. & Stone, A. D. Steady-state ab initio laser theory: generalizations and analytic results. *Phys. Rev. A* **82**, 063824 (2010).

31. Imperial college research computing service. DOI: 10.14469/hpc/2232.
32. Schreiber, W. F. Image processing for quality improvement. *Proc. IEEE* **66**, 1640–1651 (1978).
33. Huang, M. L. *et al.* Surface passivation of III-V compound semiconductors using atomic-layer-deposition-grown Al<sub>2</sub>O<sub>3</sub>. *Appl. Phys. Lett.* **87**, 252104, DOI: [10.1063/1.2146060](https://doi.org/10.1063/1.2146060) (2005).

## Supplementary Information

### Optical setup schematic

Figure S1 shows a visual schematic of the experimental setup and optical path.

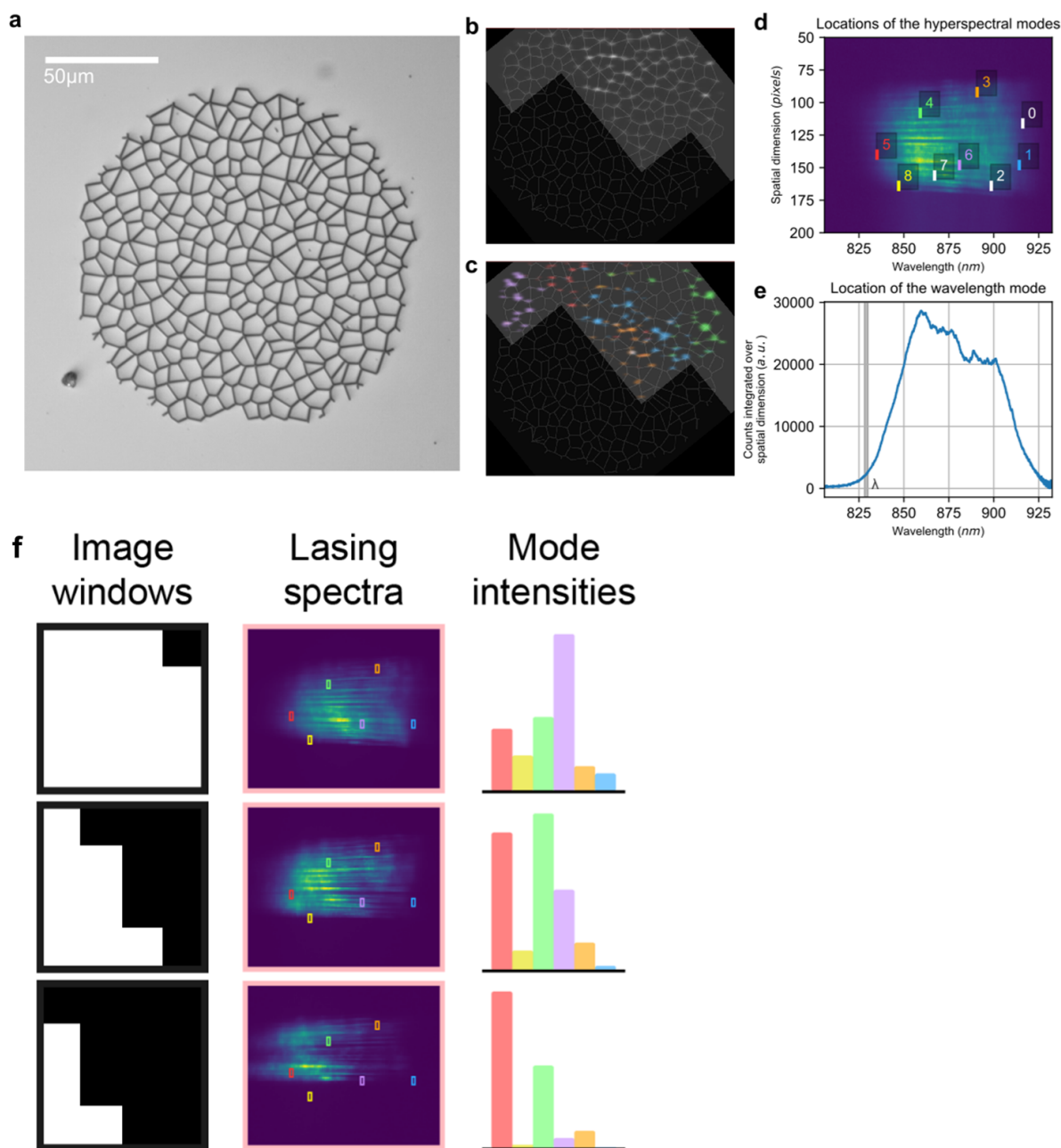


**Supplementary Figure S1.** Experimental optical setup.

### Network laser image and spectral location of feature-detecting modes

Figure S2 shows details of the InP network laser structure, spatial localisation of lasing modes and the hyperspectral regions used for feature detection. Figure S2a) shows an optical microscope image of the network used in this study. Figures S2 b) and c) show the spatial profile of the light emitted by the network in response to a spatially-structured pump illumination (dark regions of the network receive no pump illumination). Figure S2 b) shows all light emitted by the networks, figure S2 c) shows the spatial localisation of different wavelength lasing modes, with the colour-coding corresponding to the highlighted regions on the hyperspectra shown in figure S2 d). The colour corresponds to the scheme used for the mode feature maps throughout this work, eg. the red feature maps are formed via the amplitude of the hyperspectral region highlighted in red (labelled '5'). Figure S2 e) shows the spectral position of the feature-detecting mode formed by averaging over all spatial channels.

Figure S2 f) shows an example of how varying the spatial pump illumination pattern results in different lasing output responses by the network. As the spatial illumination pattern in the 'image windows' column is varied, the hyperspectral response shifts (middle column) and the amplitude of the feature-detecting modes varies dynamically depending on which image features are present (right-hand column).



**Supplementary Figure S2.** a) Optical microscope image of the InP network laser used in this study.

b) Optical image of light emitted by network under diagonal-edge illumination (dark regions of the network receive no pump illumination).

c) Optical image from b) with emitted light by the network colour-coded corresponding to the wavelength of the emitted light, with the colours corresponding to the labelled hyperspectral regions in d). Different regions of the network are seen to emit light at different wavelengths.

d) Network hyperspectral output recorded for the pump illumination pattern shown in b,c). Nine hyperspectral regions are labelled, colour-coded in correspondence with the detected feature maps used throughout this study indicating the wavelength and spatial position of the spectral regions used for feature detection. Notably, feature detecting regions are largely positioned around the edges of the main central region of hyperspectral intensity.

e) Position of the tenth feature-detecting spectral region, which is formed by averaging over all spatial channels and taking the amplitude within the indicated grey region.

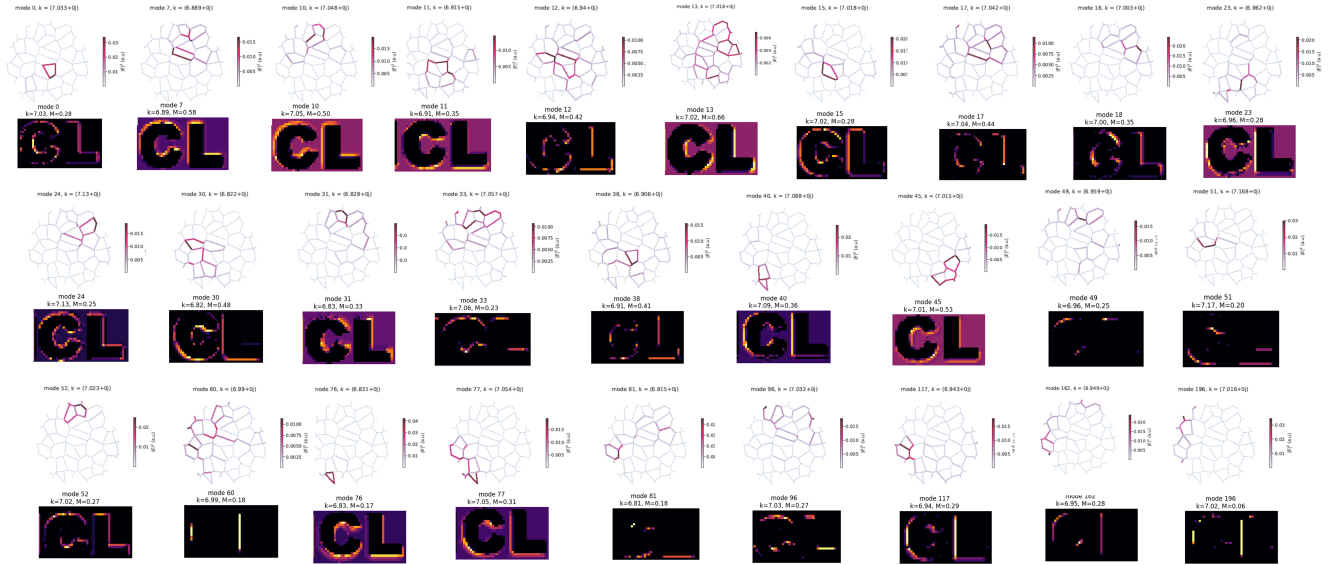
f) Varying hyperspectral response and feature-detecting mode intensities as the input illumination pattern is varied, as when windows of an input image are illuminated on the network.



## NetSALT simulated feature detection - additional feature maps and spatial mode profiles

Figure S3 shows an expanded set of 28 netSALT simulated modes, spatial mode profiles and corresponding feature maps for the CL test image. A broad range of detected image features are observed.

Figure S4 shows the full set of all 172 netSALT simulated mode feature maps. Many detected features are observed, alongside modes which only respond to very specific image regions - often lasing for only a handful of pixels of the test image eg modes 62, 157 and 109. Some modes return an output close to the input image, sometimes with enhanced lasing amplitude along a specific image feature, eg modes 2, 6, 9 and 35.



**Supplementary Figure S3.** Spectrally-multiplexed feature-maps and corresponding spatial mode profiles simulated via netSALT.

## NetSALT simulated feature detection for a regular hexagonal network

Figure S5 shows netSALT simulated lasing spectra and feature detection for a network with a regular hexagonal graph topology. The regular network shows some ability to detect features, seen in figures S5 c,d) where the system can produce different outputs between full illumination, left/right edge illumination and top/bottom edge illumination - but the regular network can not discern the difference between left and right edges or top and bottom edges. Looking at the full range of detected feature maps in S5d), a much smaller range of features are detected relative to the irregular network.

## Experimental feature detection - additional feature maps and test images

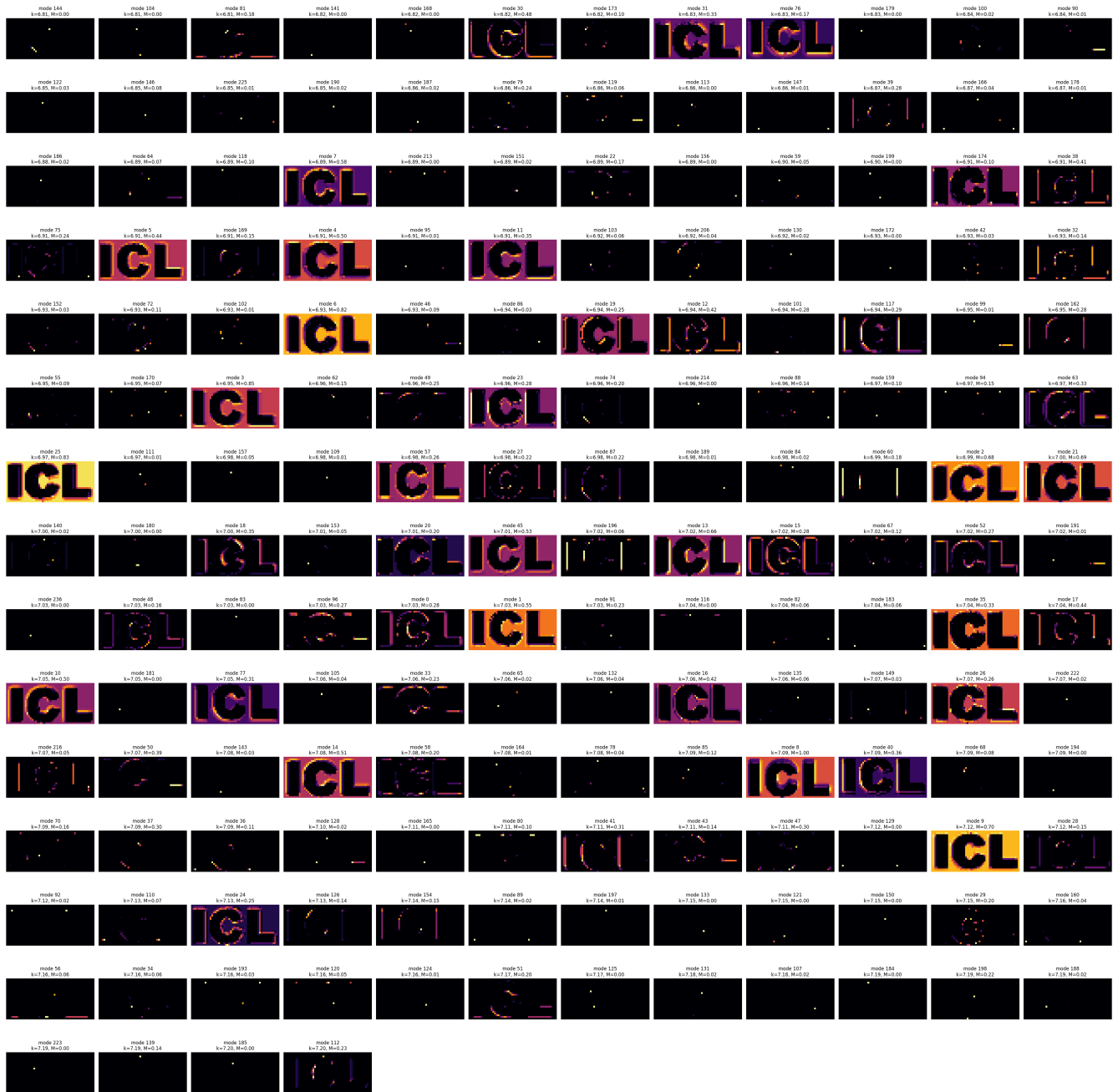
Figures S6, S7 and S8 show experimentally measured feature maps for 10 lasing modes for a range of test images to further examine the feature detection functionality.

Figures S6 and S7 show feature maps for modes 0-4 and 5-9 respectively in response to four test images: positive and negative tone circles and stars. The feature maps for these test images give a strong visual representation of the range of image features which each mode is sensitive to. Each mode responds to a distribution of similar edges, e.g. some finite arc on the circle or a range of adjacent spikes on the star. This demonstrates that the modes don't only respond to one very specific illumination pattern, but rather a distribution of similar features. This is exactly the behaviour desired for feature detection functionality, eg mode 3 responds strongly across a range of 'left' image edges, which is far more useful than only responding to a perfect vertical left edge.

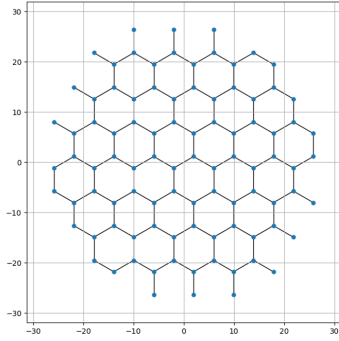
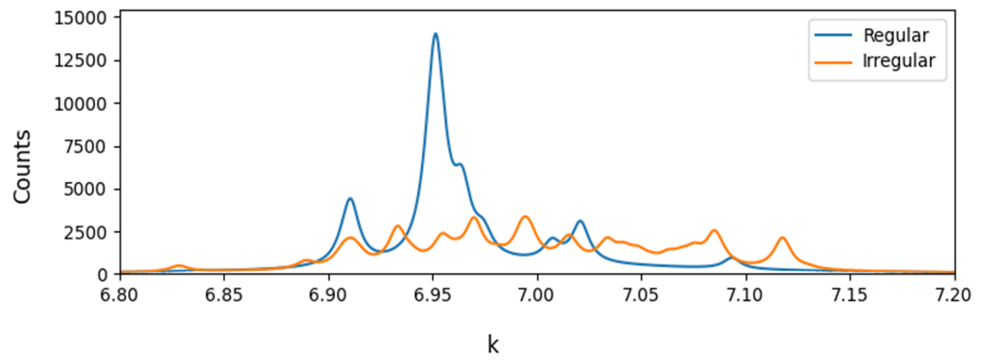
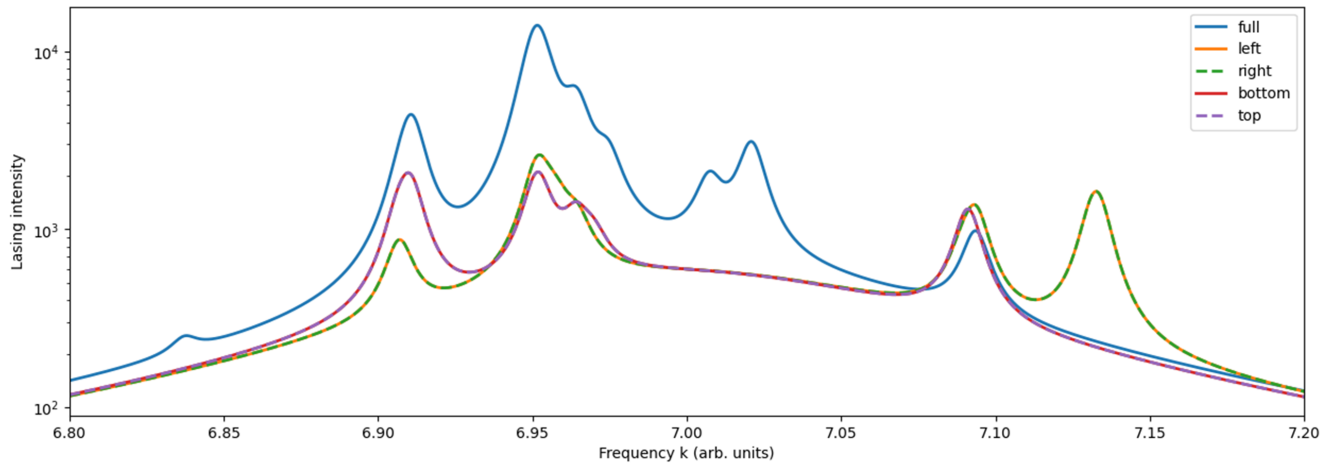
Figure S8 shows the response of modes 0-9 for a range of image edges (input images in left-most column) which are gradually rotated. This provides a good visual indication of the range of image features detected by each mode, and also shows that the ten mode provide feature detection response across all angles of image edge between them.

It is important to note that while in netSALT we can spectrally isolate the lasing response of specific modes, even if multiple modes may occupy overlapping spectral regions - this is not possible in experiment. As a result, the selected experimental hyperspectral regions and corresponding feature maps may be contributed to by more than one lasing mode.

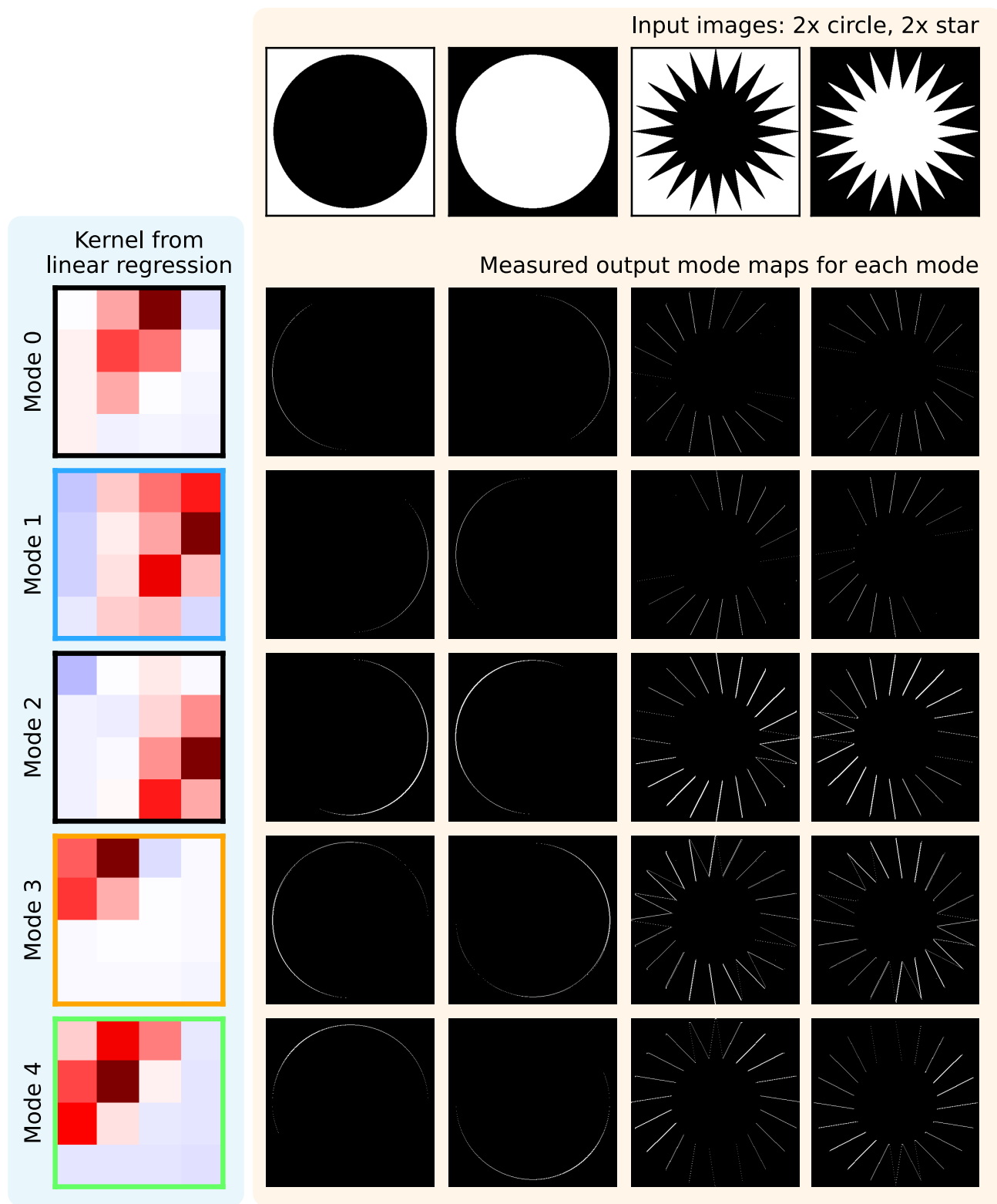
Figures S10, S11, S12, S13 and S14 show feature maps for all ten modes across the cameraman, CL and street test images, and selected MNIST-digits and Fashion-MNIST images respectively.



Supplementary Figure S4. Feature maps from all 172 netSALT simulated modes.

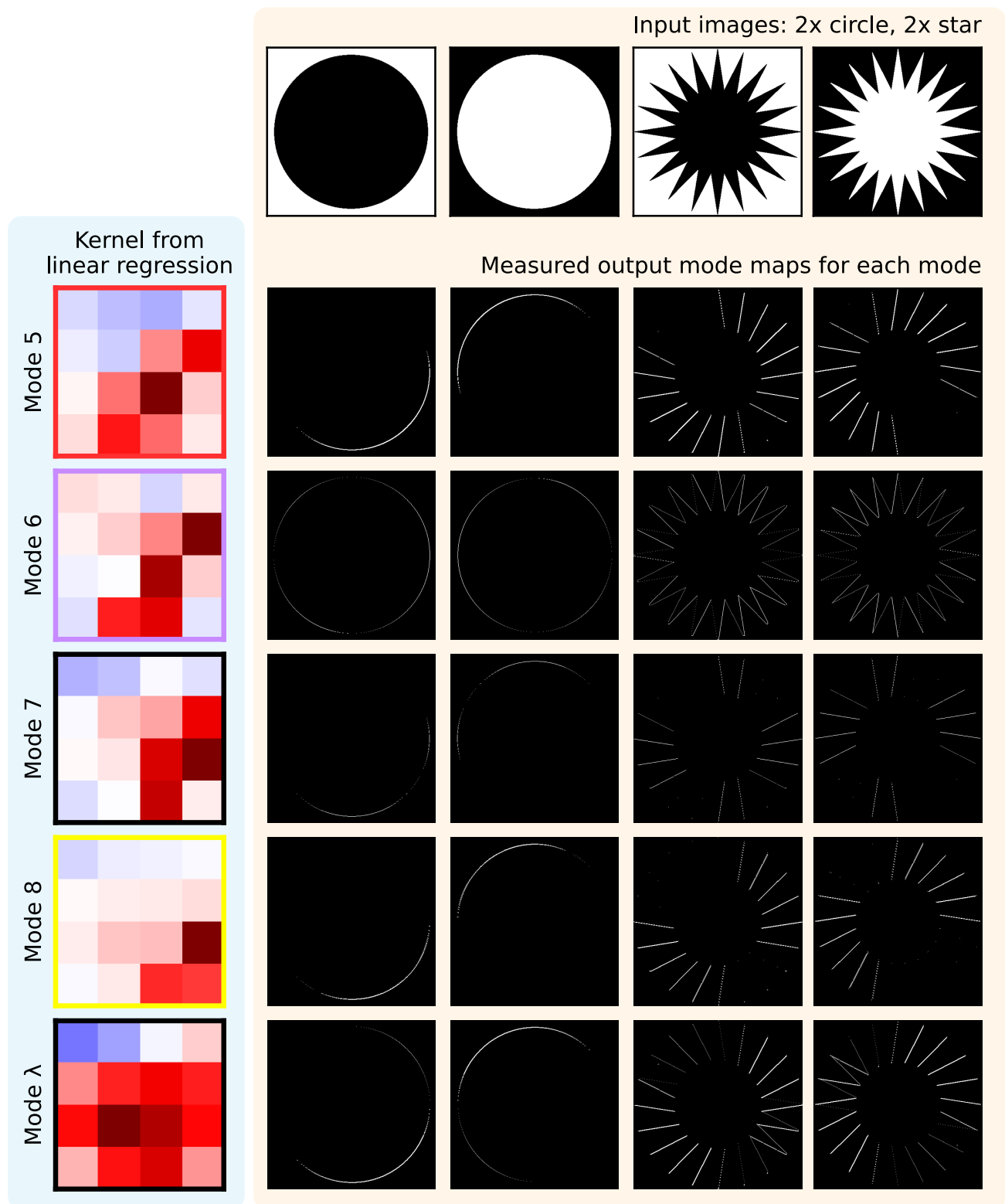
**a Regular graph topology****b Regular vs irregular graph spectra under full illumination****c Regular graph spectra under full & edge illuminations****d Feature maps of all active regular graph modes**

**Supplementary Figure S5.** netSALT simulations of a regular hexagonal network. **(a)** Regular hexagonal graph topology, 50 micron diameter graph. **(b)** Comparison of network spectra under full illumination between the regular hexagonal network and the irregular network examined in fig 2. **(c)** Comparison of regular hexagonal network lasing spectra under a variety of illumination patterns, full illumination and left, right, bottom and top edge illumination. The spectral response can differentiate between full illumination, left/right edge illumination and top/bottom edge illumination - but not between left and right edges, or top and bottom edges. The irregular network provides more sensitivity across a greater range of image features than the regular network. **(d)** Mode feature maps for all the active regular graph modes. Far fewer features are detected than the irregular graph.

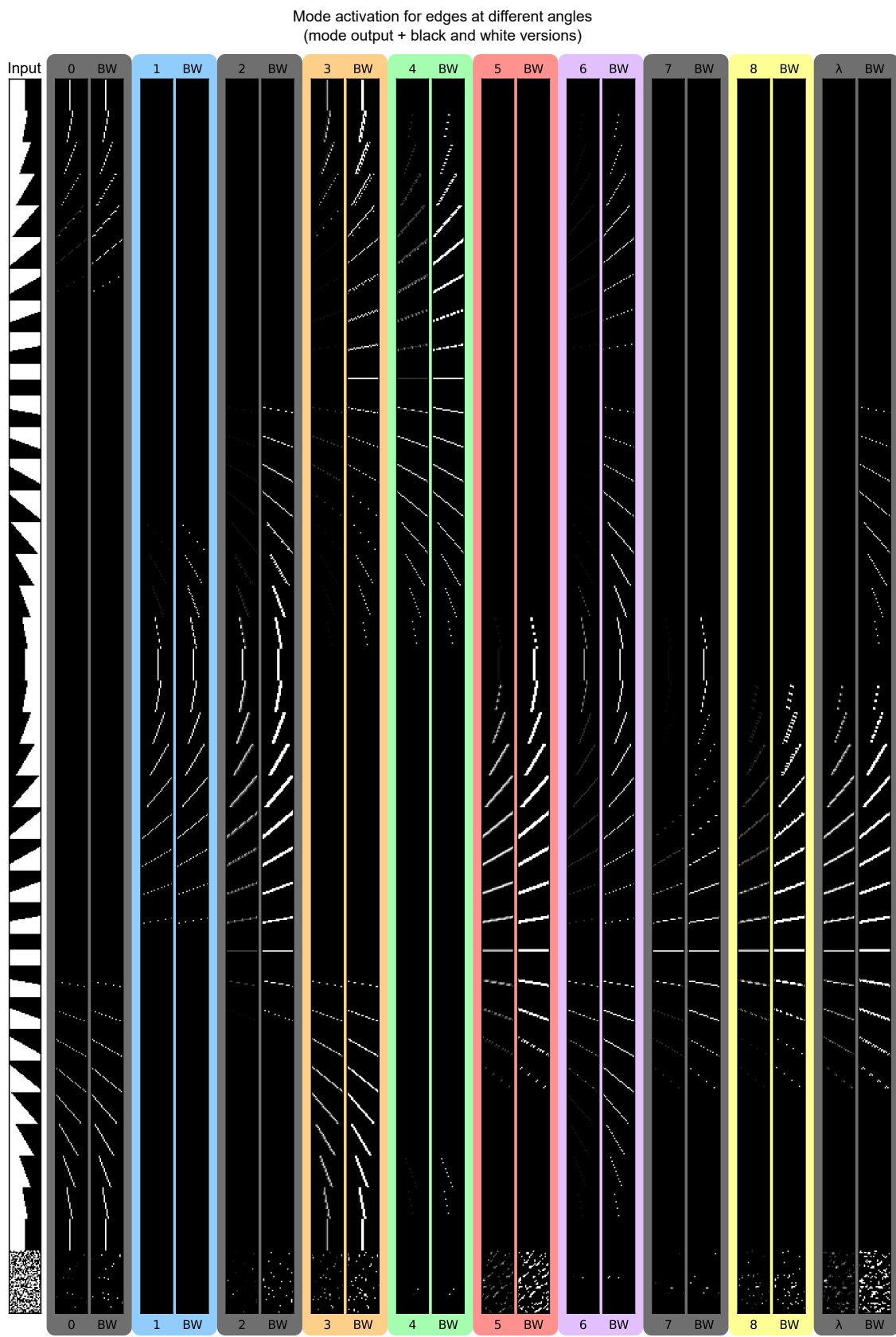


**Supplementary Figure S6.** Experimental feature maps and learned equivalent kernels for modes 0-5 on four test images, of black and white circles and stars. Each mode has a kernel displayed which was learned by comparing input images to experimentally measured feature maps, and learning the effective kernel via linear regression.





**Supplementary Figure S7.** Experimental feature maps and learned equivalent kernels for modes 6-9 (mode 9 integrates over all spatial channels, hence is labelled lambda as it contains no spatial information). on four test images, of black and white circles and stars. Each mode has a kernel displayed which was learned by comparing input images to experimentally measured feature maps, and learning the effective kernel via linear regression.



**Supplementary Figure S8.** Experimental feature maps for modes 0-9 for input images (left-most column) of a range of rotated edges, and two white noise image inputs (bottom two rows). Each mode has two columns, an analogue-varying output produced by the mode-amplitude (left column for each mode, labelled with mode number) and a binarised black and white output produced by normalising the analogue output to 0 or maximum pixel intensity (right column for each mode, labelled BW.)

### Least-squares fitting of kernel filters

As described in the main text and shown in figure 2i), we perform linear least-squares fitting between input images and feature detection output to fit effective linear kernel filters for the experimental modes performing feature detection. Results of this process are shown in figure S9. The fitting process uses a least-squares method to find the linear kernel filter weights which best reproduce the filter output (e.g. the lasing mode amplitude for our experimental case) for a given set of input images and filter outputs. As our input image set, we use the 65,536 ( $2^{16}$ ) possible  $4 \times 4$  black and white pixel images.

We plot the results of the fitting process for our ten experimental feature-detecting modes in the blue left-hand column of figure S9, titled ‘experimental fits’. For the 65,536 input images we show the target output (eg. the experimental lasing mode amplitude) and residual fitting errors in the blue and orange traces respectively in the column titled ‘mode output’ next to the fitted kernels. Substantial residual errors are observed, with  $R^2$  values of 0.628-0.946. This suggests that the linear fitting process may be unable to fully capture the feature detecting dynamics of the experimental system.

To test this assumption, we also performed the same fitting process on linear software kernel filters, initialising ten  $4 \times 4$  filters with randomly generated weights. The random kernels are plotted in the left-hand orange column titled ‘random kernels’. The results of the linear fitting process for these kernels are shown in the adjacent columns titled ‘fit’ (the kernel weights) and ‘convolved with  $4 \times 4$  images’ (target and residual errors). Here, perfect  $R^2$  scores of 1.0 are observed, as expected when performing a linear fit on a linear process. To test whether the poorer-quality linear fits to our experimental data are a result of experimental noise, we performed a further test where we added Gaussian noise to the software filter output. We used a noise amplitude of 10% relative to the maximum software kernel weights. Results of this test are shown in the two right-most columns. Lower  $R^2$  of 0.978-0.988 are observed relative to the no-noise case, but still substantially higher than the fits to the experimental data.

### Extracting effective mode kernel filters from experimental data

To compare the feature detection functionality of our system against the convolutional kernel filter approach used in software CNNs, we extracted effective kernel filters for our lasing modes. This was done by performing least-squares fitting between all possible  $4 \times 4$  pixel black and white input images (65,536 images) and experimentally measured mode amplitudes for each of the possible input images.

The results of this are shown in figure 2i) alongside  $R^2$  values for each extracted effective kernel filter. When this fitting process is performed for an arbitrary linear kernel generated in software, the fitting process performs perfectly with  $R^2$  values of 1.0. For our experimental modes, the fitting process returns  $R^2$  values between 0.76-0.95, suggesting that aspects of the physical feature detection process cannot be captured by linear matrix kernel filters.

### Quasi-isomorphic software benchmarks

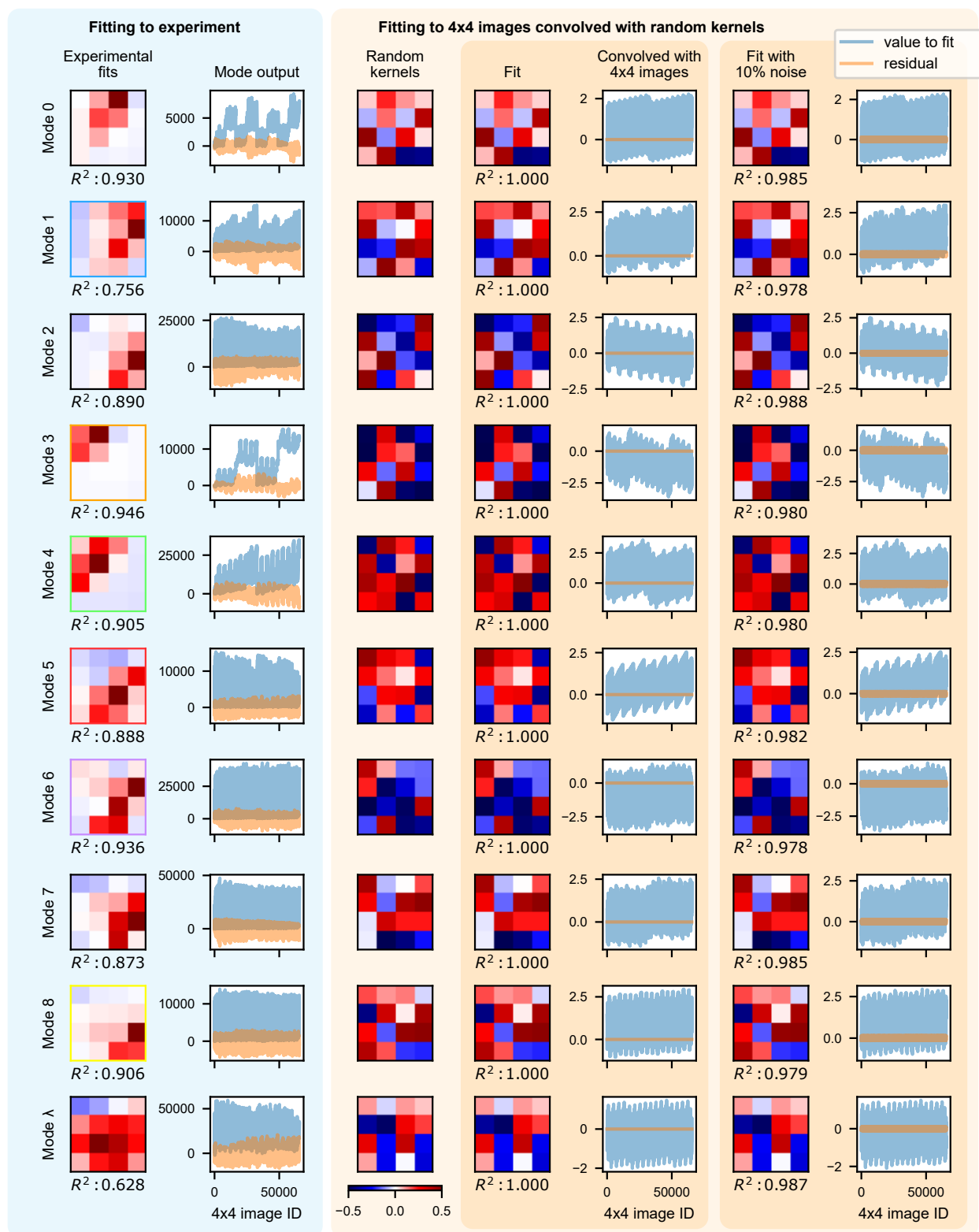
To compare our system against a software network with similar architecture, we constructed a network with quasi-isomorphic structure to our experimental system. The quasi-isomorphic software benchmark comprises an initial convolutional layer with 10  $4 \times 4$  convolutional filters, followed by a hidden layer of 30,000 neurons with randomised weights and ReLu nonlinear activation, with a final logistic regression layer. We compared our experimental system against two versions of this quasi-isomorphic software network: one with randomised kernel filter weights, and one with kernel filter weights obtained via fits to our experimental data as shown in figure 2f) and S6, S7.

Figures S15 and S16 show the classification results of these tests for the MNIST digits and Fashion-MNIST tasks respectively. The experimental photonic system outperforms the quasi-isomorphic benchmark in both cases, with the software benchmark using the fitted experimental kernel weights performing better.

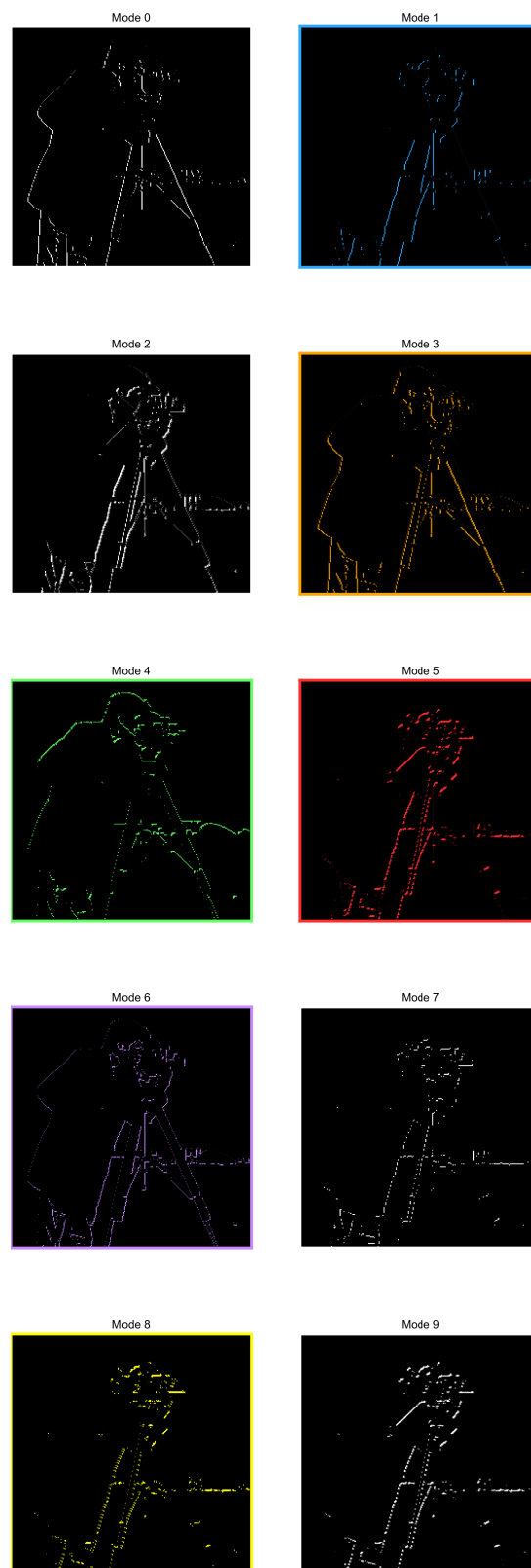
### Speed, energy and scalability

For the measurements taken in this study, each image illumination takes approximately 300 ms. As we were preparing the paper, the scheme has already been improved to run at 3 ms per image by increasing the laser repetition rate from 1 kHz to 100 kHz and decreasing spectrometer integration time, and there is a clear route to future scalability through further engineering optimisation of illumination and detection - the physical lasing dynamics of the system take 100 ps illumination. We are integrating multiple parallel processing steps in each illumination: 10 parallel feature detection processes, each with a complex nonlinear activation.

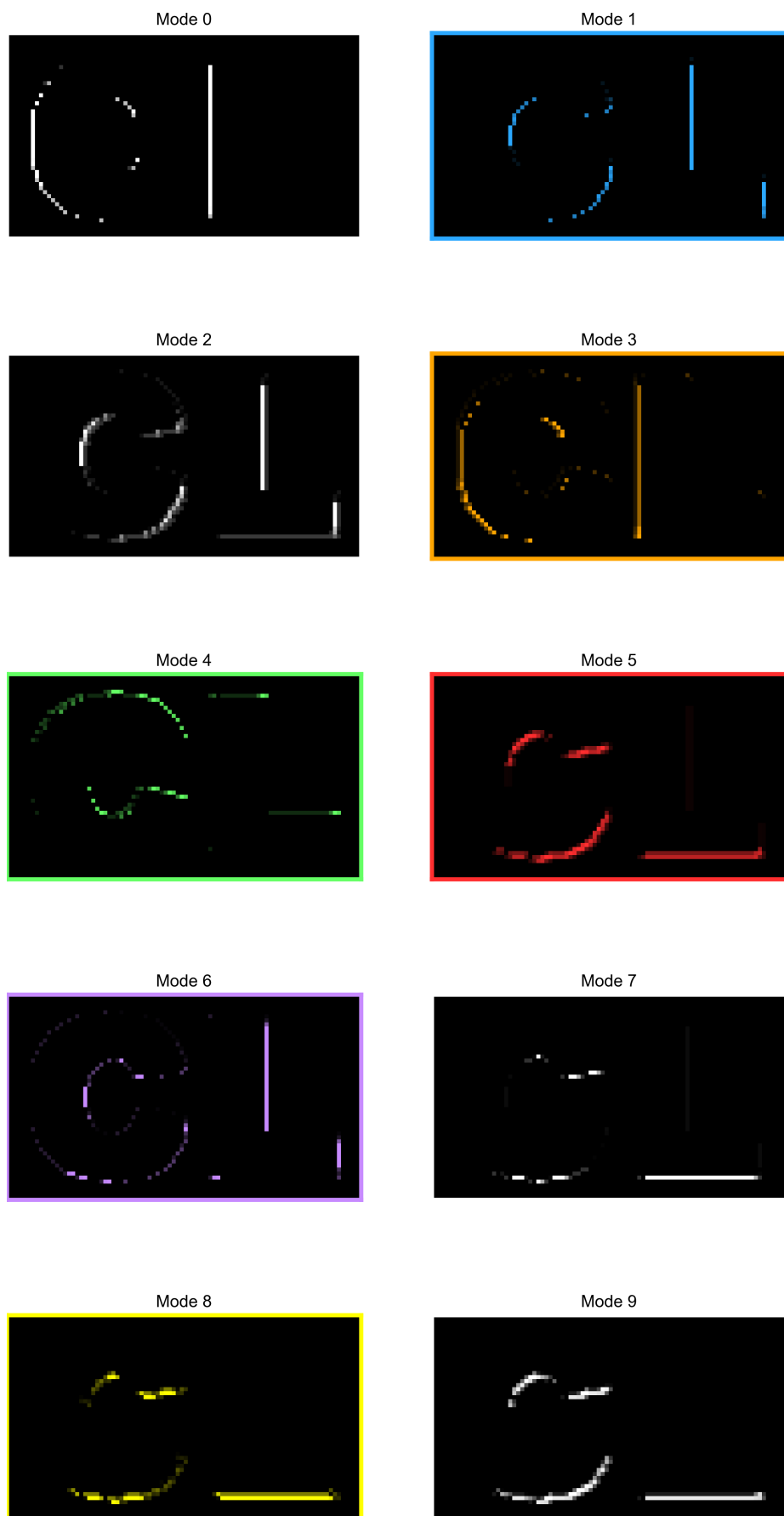
The 300 ms time per image is largely due to the fact that A) we are not using a high-speed spectrometer and are saving the data on a low-end PC without high-speed digital electronics such as a fast capture card or FPGA, and B) we operated our pump laser at a relatively low repetition rate of 1 kHz for these measurements, and integrated over 300 pulses per image to improve signal-to-noise. As mentioned above, while preparing this manuscript we have improved our experimental implementation and increased image throughput by a factor of  $100\times$ .



**Supplementary Figure S9.** Least-squares fitting of kernel filters. Left-hand blue column shows the results of the fitting process for the ten experimental feature detecting modes.  $R^2$  values from 0.628-0.946 are found, suggesting aspects of the experimental feature detection functionality are not fully captured by the linear fitting. The orange and blue mode output traces show the target value to be fitted (blue) and the fitting error residual (orange) for the 65,536 ( $2^{16}$ ) possible  $4 \times 4$  pixel images. The central orange column shows the same process performed for randomly generated linear software kernel filters, showing perfect  $R^2$  scores of 1.0. The right-hand column shows the same process performed where Gaussian noise of 10% amplitude relative to the maximum kernel weight is added, with reduced but still high  $R^2$  scores of 0.978-0.988.

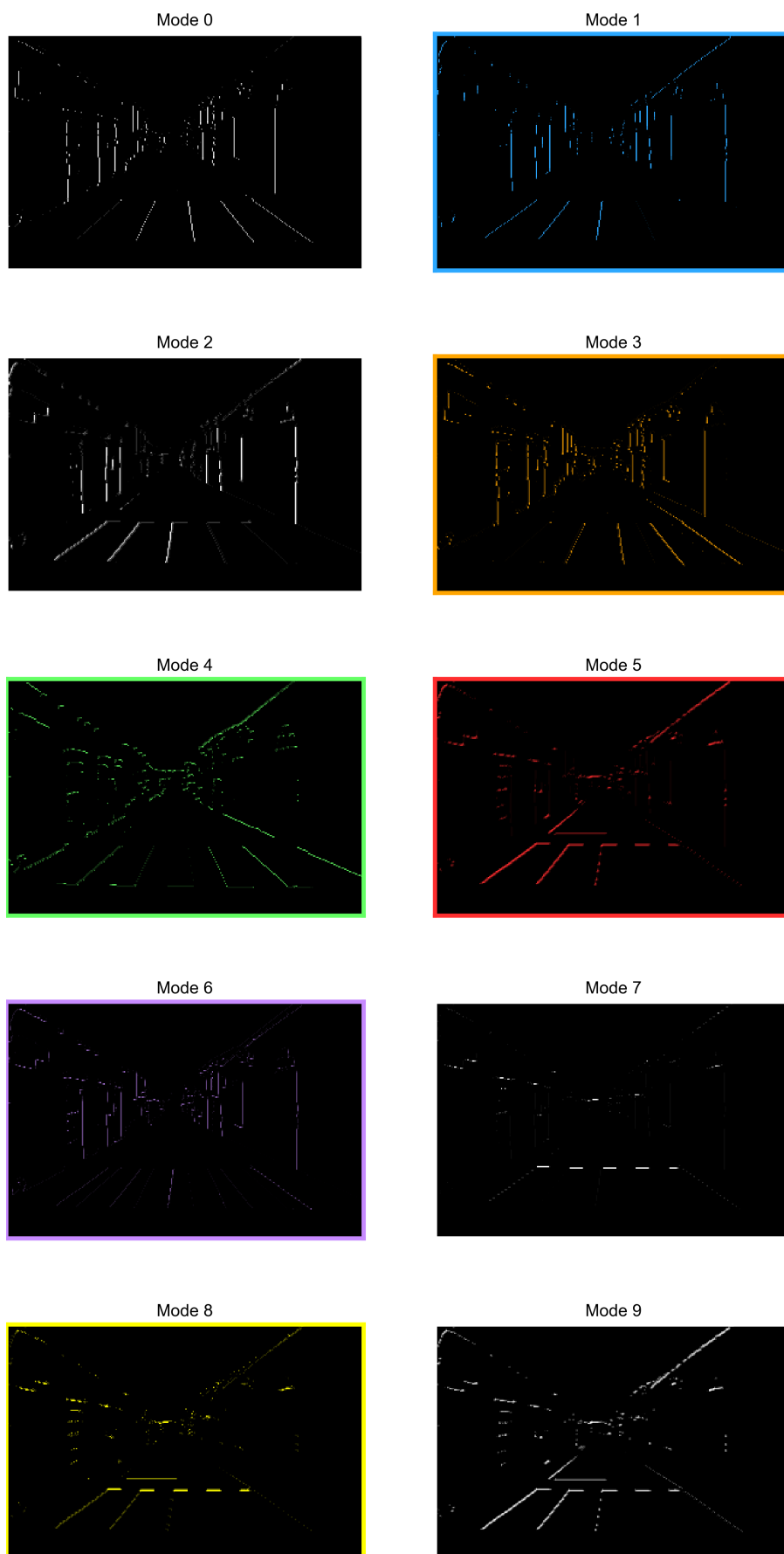


**Supplementary Figure S10.** Experimental feature maps of the 'cameraman' test image for modes 0-9.



**Supplementary Figure S11.** Experimental feature maps of 'CL' test image for modes 0-9.





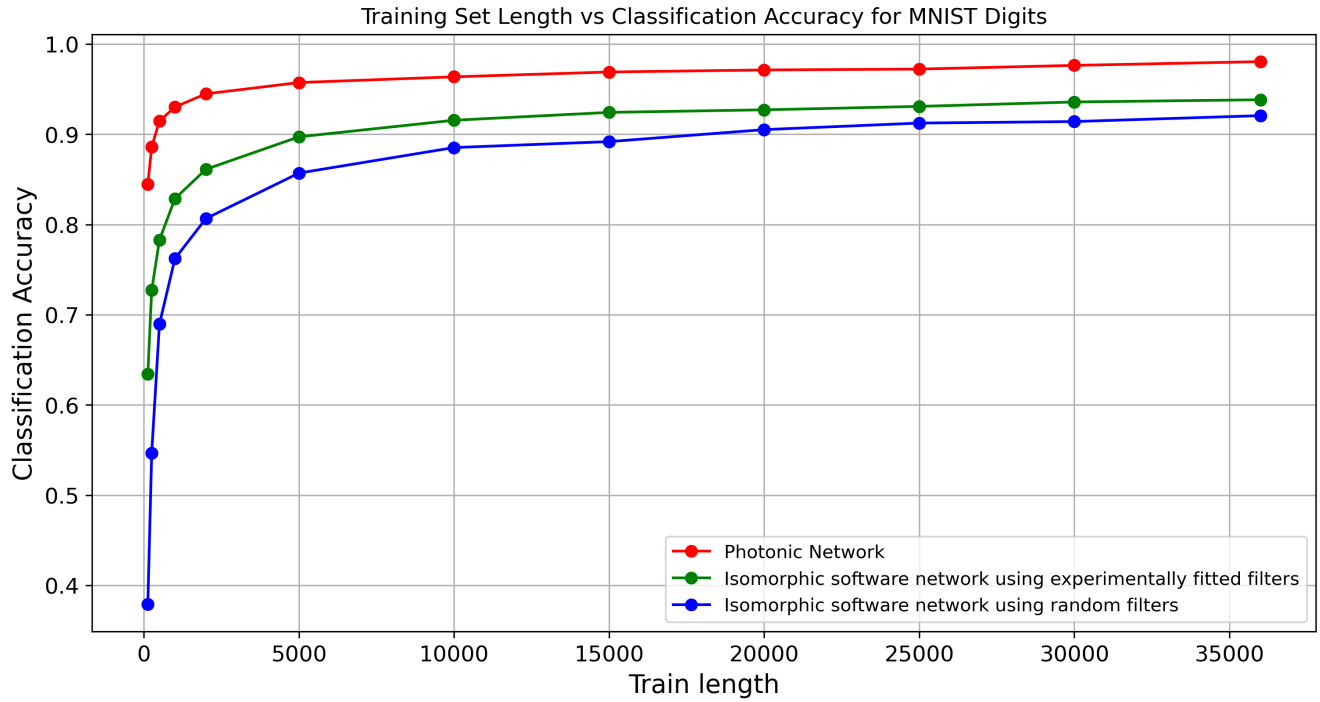
**Supplementary Figure S12.** Experimental feature maps of 'street' test image for modes 0-9.



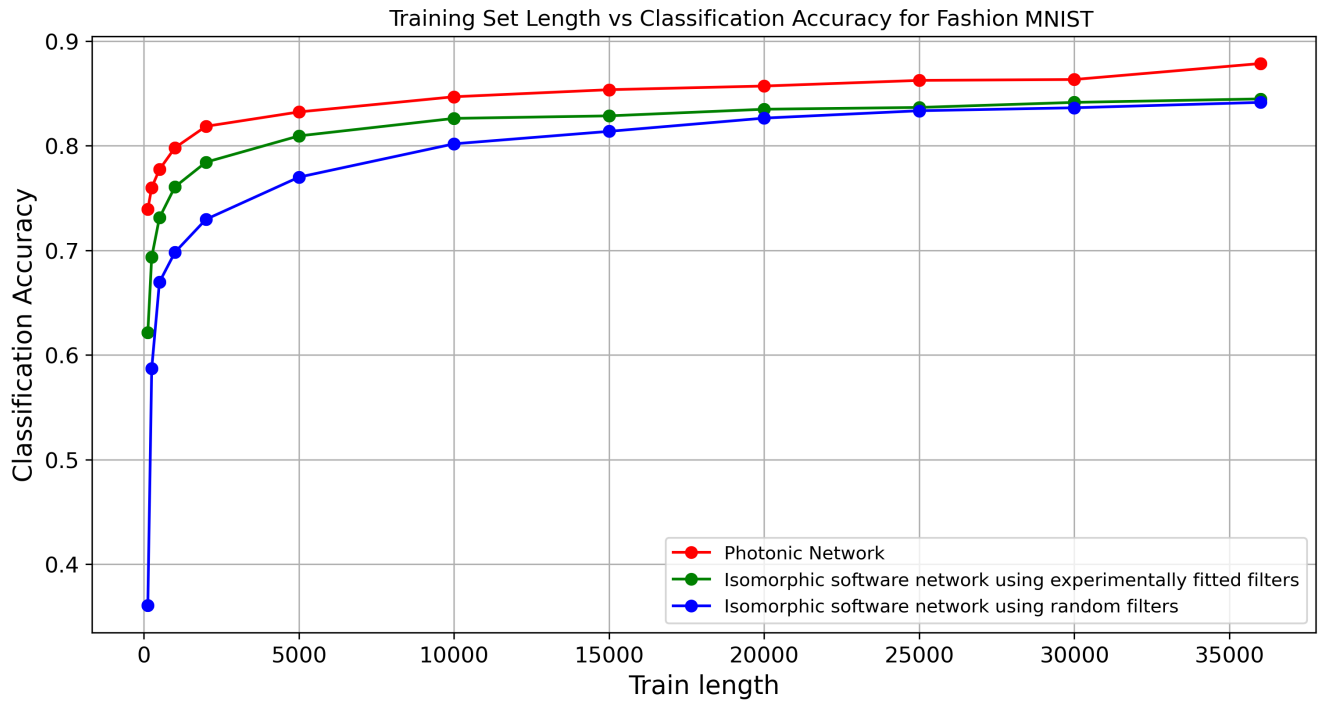
**Supplementary Figure S13.** Experimental feature maps of ten MNIST digits test images, one per digit class, for modes 0-9.



**Supplementary Figure S14.** Experimental feature maps of ten Fashion-MNIST test images, one per object class, for modes 0-9.



**Supplementary Figure S15.** MNIST digits classification results for the experimental photonic system and two versions of the quasi-isomorphic software benchmark, one with random kernel filter weights and one with kernel filter weights obtained via fits to our experimental data.



**Supplementary Figure S16.** Fashion MNIST classification results for the experimental photonic system and two versions of the quasi-isomorphic software benchmark, one with random kernel filter weights and one with kernel filter weights obtained via fits to our experimental data.

Commercially available Si or InGaAs photodiode arrays (e.g. Hamamatsu) run from  $10^4 - 10^6$  Hz and are readily integrable with our scheme. There is ample headroom for increasing our throughput via simple component upgrades and the 100 ps timescale of the key physical dynamics is attractive.

Currently we are using pump illuminations that supply 43 nJ per illumination to the InP network sample (experimentally measured via power meter). Energy consumption could be further reduced by optimisation of our network topology and geometry including lowering the system lasing threshold, for instance we found during the final stages of this work that using networks with 450 nm wide waveguides reduces the lasing threshold by around 50% relative to our existing waveguide width of 350 nm<sup>28</sup>, substantially reducing the required energy per illumination. There is scope for further reducing the lasing threshold through similar future device optimisations.